fractal and fractional

MDPI

Article

Urban Meteorology, Pollutants, Geomorphology, Fractality, and Anomalous Diffusion

Patricio Pacheco [1,*], Eduardo Mera [1], Gustavo Navarro [2] and Carolina Parodi [3]

[1] Departamento de Física, Facultad de Ciencias Naturales, Matemáticas y Medio Ambiente, Universidad Tecnológica Metropolitana, Las Palmeras 3360, Ñuñoa, Santiago 7750000, Chile; emera@utem.cl
[2] Departamento de Ciencias Exactas, Facultad de Ingeniería, Arquitectura y Diseño, Universidad de San Sebastián, Bellavista 7, Recoleta, Santiago 8420000, Chile; gustavo.navarro@uss.cl
[3] Departamento de Industria, Facultad de Ingeniería, Universidad Tecnológica Metropolitana, Santiago 7750000, Chile; cparodi@utem.cl
* Correspondence: patricio.pacheco@utem.cl

Abstract: The measurements, recorded as time series (TS), of urban meteorology, including temperature (T), relative humidity (RH), wind speed (WS), and pollutants (PM_{10}, $PM_{2.5}$, and CO), in three different geographical morphologies (basin, mountain range, and coast) are analyzed through chaos theory. The parameters calculated at TS, including the Lyapunov exponent ($\lambda > 0$), the correlation dimension ($D_C < 5$), Kolmogorov entropy ($S_K > 0$), the Hurst exponent ($0.5 < H < 1$), Lempel–Ziv complexity ($LZ > 0$), the loss of information ($<\Delta I> < 0$), and the fractal dimension (D), show that they are chaotic. For the different locations of data recording, C_K is constructed, which is a proportion between the sum of the Kolmogorov entropies of urban meteorology and the sum of the Kolmogorov entropies of the pollutants. It is shown that, for the three morphologies studied, the numerical value of the C_K quotient is compatible with the values of the exponent α of time t in the expression of anomalous diffusion applied to the diffusive behavior of atmospheric pollutants in basins, mountain ranges, and coasts. Through the Fréchet heavy tail study, it is possible to define, in each morphology, whether urban meteorology or pollutants exert the greatest influence on the diffusion processes.

Keywords: chaos; Kolmogorov entropy; geomorphology; anomalous diffusion; fractional exponent

check for updates

Citation: Pacheco, P.; Mera, E.; Navarro, G.; Parodi, C. Urban Meteorology, Pollutants, Geomorphology, Fractality, and Anomalous Diffusion. *Fractal Fract.* **2024**, *8*, 204. https://doi.org/10.3390/fractalfract8040204

Academic Editor: Carlo Cattani

Received: 23 January 2024
Revised: 11 March 2024
Accepted: 26 March 2024
Published: 30 March 2024

Copyright: © 2024 by the authors. Licensee MDPI, Basel, Switzerland. This article is an open access article distributed under the terms and conditions of the Creative Commons Attribution (CC BY) license (https://creativecommons.org/licenses/by/4.0/).

1. Introduction

Irregular phenomena are present in nature with manifestations of great complexity. As traditional geometry did not allow for their examination, a language was required to describe them. Mandelbrot gave the name of fractal geometry to this language and defined it as a semi-geometric object whose basic structure, fragmented or irregular, is repeated at different scales [1,2]. Falconer [3] defined the following properties for fractal shapes: too irregular to be described in traditional Euclidean geometric terms; it has details at any scale of observation, so, if the fractalization or the degree of detail in the geometry tends to infinity, it is impossible to measure it since the length of a fractal curve iterated to infinity, contained in a finite area, is infinite, an absent characteristic in traditional geometry; its Hausdorff–Besicovitch dimension is strictly greater than its topological dimension, and this dimension is a way of measuring the fractal dimension or fragmentation of the geometry under study and gives an idea of how it occupies the space in which it is contained; and it has self-similarity, whether exact, quasi-self-similarity, or statistical, since it is created from a recursive method developing complex structures, which is the reason for the abundance of fractals in nature (geological processes, development of biological structures, etc.). Figure 1 shows geomorphologies with a fractal design:



Figure 1. Three fractal geographies.

Urban meteorology time series, characterized by temperature (T), relative humidity (RH), and wind speed magnitude (WS), are chaotic and have a fractal dimension (D) [4]. Urban meteorology interacts with geographical morphologies that admit a fractal representation (basin, mountain, coast). In this natural context, an element of disturbance that is also chaotic and fractal has been incorporated: pollutants (considered in this research as PM_{10}, $PM_{2.5}$, and CO), which act as an element of artificial fractal disturbance on geography and meteorology. Pollutants, emitted and sustained by humans, are conducted in a similar way to a dissipative system. If the initial condition is associated with a primitive equilibrium, increasing disturbances can no longer be absorbed by the system. The system stabilizes in a state far from the initial equilibrium, creating a dissipative structure (Manríquez, 1987) which is not stable either [5].

The use of fractals is present in the normalization and classification of city shape indices, which is a recent topic of research [6,7]. In general, shape indices are not effective given the uncertainty of spatial measurements such as perimeter and area [8–13]. The uncertainty of geographic measurements is always associated with the fractal properties of geographic systems [14,15]. Fractals suggest the optimal structure of natural and human systems. A fractal object can occupy space in the best way. It is possible that, by using the ideas of fractals to design cities and city systems, the geographical environment and natural resources could be used sustainably [6]. It can also be argued that, if the layer of human buildings was fractal, it would plausible for fractal cities to disturb the interaction between fractal natural geography and fractal meteorology, generating another source of disturbance in the atmosphere which will further contribute to climate change. A possible fractal city should be the self-similar continuity of a fractal basin, mountain, or coast. Just as cities are human products so is garbage (gaseous, liquid, or solid), until now an insolvable problem.

Mandelbrot [2] defined the fractal dimension as a non-integer value, which allows the description of fractal geometry as well as the heterogeneity of irregular figures, capturing the information which is lost when using traditional geometry representations [4]. The fractal dimension (D_F) is related to the Hurst exponent (H) through the following equation, developed by Voss [16,17]:

$$2H + 1 = 5 - 2D_F \quad (1)$$

From the previous equation, we can obtain the following:

$$D_F = 2 - H \quad (2)$$

A fractal landscape, real or imagined, is produced using fractals. Essentially, you subdivide a square into four equal squares and then randomly shift their shared center point. This process is repeated recursively on each square until the desired level of detail is reached. While fractal landscapes appear natural at a first glance, natural processes such as erosion in mountains are not observable. In this way, simple fractal processes do not reproduce geological functions (geophysics, tectonics, structural geology, stratigraphy, historical geology, hydrogeology, geomorphology, petrology, and pedology) and real climatic functions (interaction with oceans, vegetation, humidity, rotation of the earth, etc.).

1.1. Indicators of Boundary Layer Disturbance

The scientific community recognizes that the manifestations of climate change are given by indicators such as the concentration of greenhouse gases, the rise in sea level, ocean heat content, and ocean acidification. These indicators recorded unprecedented values in 2021, a trend which continues to date. According to the World Meteorological Organization (WMO), this is a new clear example that human activities are causing changes on a planetary scale: on land, in the ocean, and in the atmosphere. These changes have harmful and lasting repercussions for sustainable development and on various ecosystems [18–21].

The extreme climatic conditions arising from the effects of climate change have caused a loss of human life, alongside economic losses, and have seriously undermined people's well-being [22], all consequences which have worsened [23–29]. This large-scale problem [30,31] of apparently irreversible and large-magnitude alterations has a horizon of low predictability. This research is focused on the microscale, the place of human activity, within the boundary layer [21], which is showing a similar behavior.

The construction of good indicators that account for processes in natural environments (atmosphere, land, sea) is closely related to their measurement. On large scales, for example, it seeks to estimate trends and variability in lake water storage (LWS) at a global level. The satellites that orbit the Earth carry out, through sensors, repeated observations of the surface and water level in lakes, providing data which allow one to evaluate changes in water accumulation. Several difficulties affect these observations—sensors, their resolution, infrequent satellite transit, very separated observation orbits, discontinuity in missions, etc.—complicating the comprehensive record of lake water storage variations [22]. This measurement problem is even greater in the boundary layer, given its small thickness (in the order of 1000 to 2000 m, depending on the time of the measurement) and due to the notable influence exerted on it and its turbulence by the natural or artificial roughness of the surface of the Earth. This is the reason why, for this case, the measurement on the surface itself, with an adequate density of sensors in situ, cannot be replaced by satellite or simplified simulations that use one-dimensional models.

1.2. Urban Meteorology and Pollutants in the Boundary Layer

Urban heat islands occur in parts of the city that experience higher temperatures than the periphery due to people's activities. The reason for this are the components of the Earth's surface energy flux $Q^* + Q_F = Q_H + Q_E + \Delta Q_S + \Delta Q_A$, where Q^* is the net radiation, Q_F is the anthropogenic energy release into the control volume, Q_H sensible heat flux, Q_E is the latent heat, ΔQ_S is the accumulated heat flux within the control volume element that includes air, trees, building materials, and soil, and ΔQ_A is the net advection through the lateral sides of the control volume [32–34]. It is difficult for impermeable surfaces to present the cooling effects driven by latent heat, adding to this the production of heat and pollution from industry and traffic, increasing the effects of climate change [35–39]. For two decades, in relation to climate change in Chile, heat waves have appeared, more intense and of a longer duration, focusing on the center of the country, which contains the capital of Chile, in an area with a basin geography. The Climate Evolution Report in Chile 2021, from the Chilean Meteorological Directorate, indicates that the past decade was the warmest on record. Chile's strategy (for 2050) is summarized in [40]. Human activity modifies the initial conditions of the environment and geography (even with small disturbances), with great effects on nature and population health in the very short term [41].

For air pollution, indicators of its effects on human health have been developed: eye irritation, respiratory tract diseases, heart diseases, brain disorders, etc. [23–29]. For the atmospheric layer adjacent to the ground, the boundary layer, it is relevant to have long-period indicators, because all atmospheric events, such as rainfall, the seasons of the year, the formation of low clouds, the coastal trough, the interaction of vegetation with the surface atmosphere, etc., occur in that layer [21]. These events show an increasing and complex connectivity with human activity [22,30,42]. The Earth's natural geographic roughness has been an element of climate modeling for millions of years [31,43]. Furthermore, the

geographical morphologies of basins, coasts, or mountains affect the values of meteorology and pollutant measurements [31,43].

This research locates the hourly measuring instruments that deliver time series of large periods of an urban meteorology system (T, RH, and WS) and a pollutant system (PM_{10}, $PM_{2.5}$, and CO) in areas with coastal, mountainous, and basin geomorphologies, the latter being that of Santiago de Chile. The geography of a city contains surface roughness of different levels, referring to the sea, which are used to locate the above-mentioned instruments. Polluting system affect the urban meteorological system and the boundary layer, giving rise to interactive processes which are irreversible, turbulent, with a low predictability, and chaotic in general, making it appropriate to study them with chaos theory [43].

1.3. Kolmogorov Entropy (S_K) and Loss of Information (<ΔI>)

Entropy is a variable that allows one to study the disorder associated with long-term processes and adjusts very well to a chaotic analysis that requires series of very large amounts of data (over 5000 data points due to the requirement of stability in the calculation of the Lyapunov coefficients). Entropy is a fundamental variable of nature that has been investigated and applied in many different areas, but its application to the study of communications, urban dimensioning, fluids, the Earth atmosphere system, medicine, biology, etc., is relatively recent [44–47]. However, its application to pollutants and the interaction with the atmosphere in the boundary layer is much more current [48,49].

Chaotic itineraries permanently produce current information, while predictable routes do not [50–52]. Kolmogorov–Sinai entropy (or metric) gives an upper limit to the information gain ratio. The definition of metric entropy is due to Shannon [53], and, later on, it was applied to dynamical systems. Kolmogorov [54] and Sinai [55] proved that it is a topological invariant (K-S entropy) [56–58].

According to Shannon, entropy is the rate of creation of information when a chaotic system evolves; it is positive and can reach large values. Its evolution is thought of as a loss of information; predictions from the initial state are more imprecise over time. If two points of a spatial state, very close, are separated in time, then they depend on the initial conditions. As time passes, more will be known about the initial condition as the initially non-significantly differentiated digits make themselves felt [59].

An information source can be considered as a Markovian process, randomly generating one n symbol at discrete times [56,60]. For example, this text constitutes a Markov process. The symbols may be the result of sequential measurements [50]. In a process of order mth, the sequence that includes the previous $m-1$ symbols, ($x_1\ x_2 \ldots x_m$), can be described as the fraction m digit base n $x_1\ x_2 \ldots x_m$, abbreviated to Xm, a value which specifies the state of the source (not the state of a dynamical system) [52].

A numerical sequence, which is the result of measurements, can be considered as symbols emanating from a Markov source [50]. A measurement at time t = 0 specifies that the state of the dynamic system is somewhere within a specific element of the partition. At a finite time Δt later, another measurement may give another result, revealing that the state is in another element of the partition. In this way, a sequence of measurements produces a chain of symbols. The information rate per unit of time for this sequence of symbols in the limit with $m \to \infty$ is $\Delta Im/m\Delta t = \Delta l/\Delta t$. The entropy metric is the maximum information ratio when changing the partition and the sampling ratio [55]:

$$h_\mu = \underbrace{\sup}_{\beta,\Delta t} \lim_{m\to\infty} \left\{ \frac{I_m}{m\Delta t} \right\}, \tag{3}$$

If an observer measures it with ideal instruments and at an ideal usage speed, metric entropy is the average of new information for each sample.

A dynamical system has a trajectory of $x(t) = [x_1(t), x_2(t) \ldots x_d(t)]$, in a phase space of dimension d. As Figure 2 shows, by dividing the space into boxes of size l^d, with d as

the dimension of the space, measuring the state of the system at regular times τ, the joint probability of the system, Pi, is related to the instant t = 0 in box i_0, t = τ in box i_1, and nτ in box i_n. The magnitude Kn is defined as follows [53]:

$$K_n = -k\sum_i^n P_i \log P_i, \quad (4)$$

where the quantity is proportional to the information necessary to locate the system on a specific trajectory that transits the $i_0 \ldots i_n$ boxes, with low uncertainty. The coefficient k is employed for the choice of the unit of measurement.

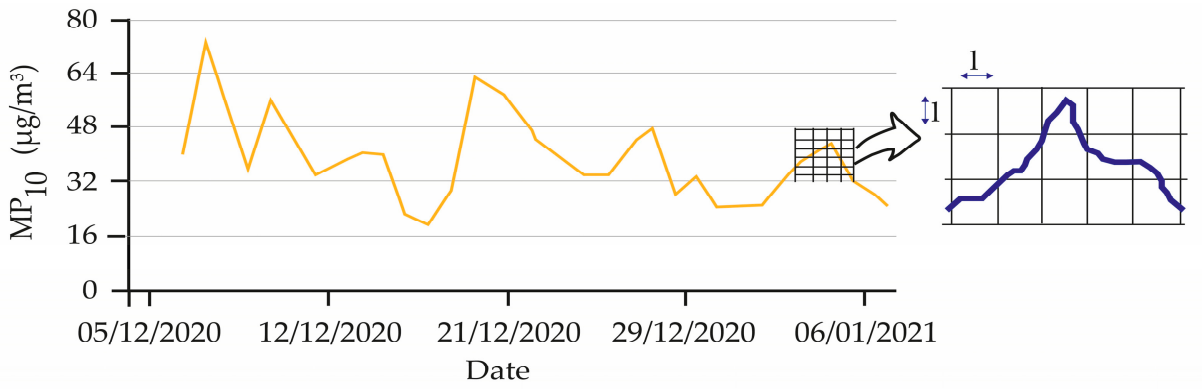


Figure 2. It shows the temporal evolution of the concentration of 10 µm of particulate matter (as an example). In blue, the trajectory is in a phase space where there are n boxes with sides l.

The additional information necessary to know in which cell i_{n+1} the system that was previously in $i_0 \ldots i_n$ will be found is $K_{n+1} - K_n$. This is also the loss of information of the system when evolving from nτ to (n + 1)τ. S_K is the average information loss when $l \to 0$ and $\tau \to 0$:

$$S_K = -\lim_{\tau \to 0} \lim_{l \to 0} \lim_{n \to \infty} (n\tau)^{-1} \sum_{i=1}^{n} P_i \log P_i, \quad (5)$$

S_K has units of information bits per second and bits per iteration in the case of a discrete system [61,62]. In summary, if S_K is (a) $0 < S_K < \infty$, it denotes a chaotic behavior; if it is (b) 0, no information is lost, and it is a regular and predictable system; and, if (c) $S_K \to \infty$, the system is completely random and not predictable.

The average loss of information (I) in [bits/h] [52] is as follows:

$$< \Delta I > = < I_2 - I_1 > = \frac{-\lambda(x_0)}{\log 2}, \quad (6)$$

I_1 and I_2 are old and new information, respectively, and λ is the Lyapunov exponent. The Lyapunov exponent, $\lambda(x_0)$, represents the exponential separation between two trajectories, initially close, after N steps or iterations, and contains a quantity of information I referring to that separation $I(x_0)$. Due to notation considerations, $\lambda_0 = \lambda(x_0)$ remains as follows:

$$< \Delta I > = \begin{cases} \to 0, \text{rapid loss of information, chaotic system} \\ \to \text{large values, slow loss of information, more predictable system} \end{cases} \quad (7)$$

There are two categories of chaos indicators: (1) those which measure the loss of information during evolution (λ, S_K); and (2) those referring to the fractal nature of the signal or attractor. For this research, (1) was applied. Two types of <ΔI> were calculated, one for the pollutants and the other for the urban meteorology considered in this study [42].

The basic equation constructed and used was the following:

$$C_K = S_{K,MV}/S_{K,P} = \left(\sum S_{K.MV,i}/\sum S_{K.P,i}\right)_{COMMUNES} \quad (8)$$

The numerator contains the sum of the entropies of each meteorological variable (T, RH, and WS). The denominator includes the sum of the entropies of each pollutant (PM_{10}, $PM_{2.5}$, and CO). C_K is one per commune (located at different heights, with their monitoring station). C_K is dimensionless and is an entropic comparative index of the two interacting systems over a period of 3.25 years.

1.4. History of Applications of the C_K Parameter

This research uses the C_K parameter, whose behavior was examined in six measurement stations, located at different heights with respect to the sea level, in three periods (2010–2013, 2017–2020, and 2019–2022) of 3.25 years each [63–69], in the geographic basin of Santiago de Chile. The presence of confinements due to the SARS-CoV-2 pandemic, in period of 2020–early 2022, with the reduction in labor in Santiago, Chile, was an occasion to analyze C_K due to the probable variations in urban meteorology and pollutants [43]. The effect of the polluting system on the urban meteorological system is checked by calculating the entropies [64,65] in the time series. The series are localized and contain a history that includes the seasons of the year (autumn, winter, spring, and summer), with droughts, heat waves, heavy and unusual rains, geographical aspects, human activity, etc. The measurements carried out have two widely separated periods (2010–2013 and 2017–2020) and two close periods with partly overlapping data (2017–2020 and 2019–2022, last measurement). In the construction of C_K, measurements from two other countries (Mexico and Ecuador) were also used in order to investigate its sensitivity in different contexts of human activity and geographical morphologies, such as mountains and coasts [43]. The behavior of C_K in the geographic basin of Mexico City is similar to that in Santiago de Chile (less than 1), changing (greater than 1) in coastal locations in Chile and in mountain locations in Chile and Ecuador [43]. Santiago de Chile matters as it concentrates 42% of the country's population. In Chile, according to the measurements carried out, C_K declined from 2010 to the present. This gives a vision of atmospheric deterioration, with strong variations close to the ground, due to human activity. The characteristics of C_K are compatible with a Kolmogorov cascade-type behavior: high turbulence in the vicinity of the ground which attenuates with height [66,67]. The roughness of the Santiago de Chile basin makes it possible to place instruments for measuring urban meteorology and pollutants at different levels, showing that the entropic interaction between them, according to C_K, changes over time [68].

With C_K one can study the boundary layer and the disturbances that affect it [54], showing the following: sensitivity to turbulence near the ground; who exerts a greater influence between urban meteorology and pollutants by calculating the Kolmogorov entropy for each variable; the asymptotic decay of turbulence with height, consistent with a Kolmogorov cascade-like behavior; in three dimensions, the areas of the highest C_K density, the interactive phenomenon of urban meteorology–pollutants and entropic forces; the evolution of C_K over time by measurement periods; the existence of thermal effects in the form of flows; sensitivity to events (pandemic, urban densification, heat waves, thermal islands, fires, etc.); its behavior in three geographies, i.e., basin, coast, and mountain range; the presence of resilience and sustainability according to the initial conditions of the study area; and how entropic flows and vertical wind speeds favor polluting "contagion" between cities, to the detriment of urban meteorology. All these are characteristics that also reveal the impact of the interaction between the surface changes induced by urbanization and air pollution on the urban climate [69,70].

The time series were extracted from three monitoring networks: in Chile, from SINCA (National Air Quality Information System) [71], whose data are public; in Mexico, from SINAICA [72]; and, in Ecuador, from SUIA [73]. These networks perform real-time measurements of meteorology and pollutants, have a proper distribution, and are reliable and according to international standards, operating for long periods (years) without interruption.

1.5. Anomalous Diffusion

In recent times, many physical and biological systems have been found in which the average square displacement traveled by the diffusing substance grows with time in the form of $< r^2 (t) > \propto t^{\alpha}$, where the value of the exponent divides the processes diffusive in two different ways: superdiffusion for $\alpha > 1$ and subdiffusion for $\alpha < 1$, both particular cases of what is called anomalous diffusion, Figure 3.

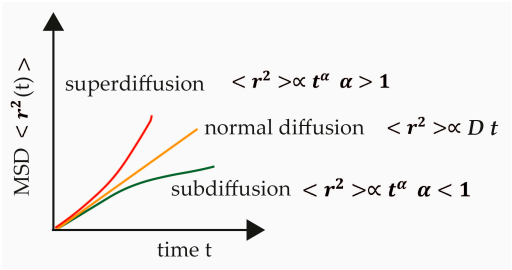


Figure 3. Mean square displacement of anomalous and normal diffusions.

Anomalous diffusion has applications beyond physics. It allows one to describe and model various complex systems such as the internal structure of living cells [74] and the way in which different species of animals find food [75] and specify the movement of water or oil in highly disordered reservoirs [76].

1.5.1. Types of Anomalous Diffusion

Statistical physics studies cases that give rise to anomalous diffusion: extended correlations [77], CTRW [78], fBm [79], diffusion in fractals [80], and diffusion in heterogeneous media [81]. Some of the most studied anomalous diffusion processes are the following [82,83]: (i) generalized Brownian motion of the fractional type [82,83] and the scaling type [83]; (ii) diffusion in fractals and filtering in permeable media; (iii) walking randomly in continuous time; and (iv) many other fields [84–91].

1.5.2. Anomalous Diffusion Is a Nonlinear Process

In statistics, normal (physical) diffusion is defined as in [92–94], Appendix A:

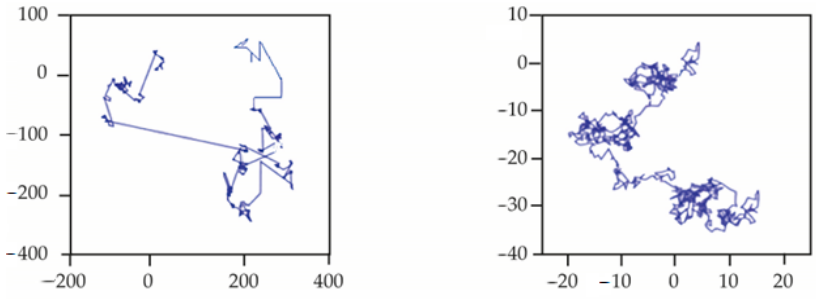
$$< x^2 >= 2Dt \tag{9}$$

where $<x^2>$ is the variance of the distribution in the position of a particle moving on a plane, D is the diffusion coefficient (measured in the International System in m^2/s), and t is the time. The graph between $<x^2>$ and $x = \bar{v}t$ (where v means velocity, and t is the growth over time of the dispesivity) is a straight line. This type of diffusion is totally defined by the diffusion coefficient. If the diffusion coefficient is treated as a variable and calculated through an experimental procedure,

$$D = \frac{< x^2 >}{2t} \tag{10}$$

where the ratios of $<x^2>$ and t are expected to be constant.

If certain random walks are considered, such as in Figure 4, there are some that are known as Lévy flights, and the diffusion constant becomes infinite, which implies that this is not the type of walk considered in the central limit theorem. There are cases where Lévy flights lead to anomalous diffusion: the variance grows faster than in a linear function.



(a) (b)

Figure 4. (**a**) 1000 steps of a Lévy flight in two dimensions; and (**b**) 1000-step example of an approximation to a two-dimensional Lévy flight type of Brownian motion.

During anomalous diffusion the diffusion relationship is the following [95,96]:

$$< x^2 > \sim D_\alpha t^\alpha \tag{11}$$

where α is the so-called anomalous exponent. For $\alpha < 1$, the process is subdiffusive, and, for $\alpha > 1$, the process is super-diffusive. When calculating the ratio of $<x^2>/t$ during an abnormal process, then the following holds true:

$$D_{app} = \frac{< x^2 >}{t} \sim D_\alpha t^{\alpha-1} \tag{12}$$

The instantaneous value of the apparent diffusion coefficient D_{app} changes with time. This means that there is no constant value that defines the diffusion of the particles in the medium, the system is not in thermal equilibrium, and the classical laws of diffusion are not fulfilled. In this case, the anomalous exponent becomes more important. The cause of this disagreement is the conjecture made in Equation (9), according to which the Brownian particle moves in a uniform infinite medium which functions as a thermal bath. This assumption is generally incorrect if the Brownian motion occurs in a complex medium, such as in a fractal geographic morphology or in a turbulent boundary layer near the ground. The equation that describes anomalous diffusion is a power law. In power laws, there is no single time constant, as in any process described by an exponential decay. A power law arises from the sum of an infinite number of sums of processes with different time constants. $D\alpha$, in Equation (11), has the dimension $[D\alpha] = cm^2 s^{-\alpha}$. According to the value of the anomalous diffusion exponent α in Equation (11), one usually distinguishes several domains of anomalous transport, as sketched in Figure 5.

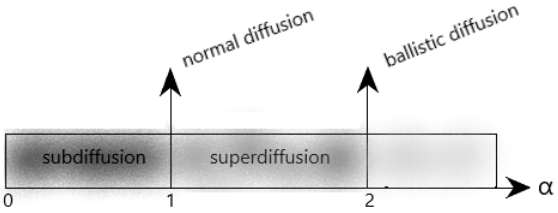


Figure 5. Anomalous diffusion, according to the mean square displacement, Equation (11), with subdiffusion for $0 < \alpha < 1$ (left area of the figure) and superdiffusion for $\alpha > 1$ (from the intermediate area to the right of the same figure). At the limit between both zones is the normal Brownian diffusion (special case: ballistic motion ($\alpha = 2$)).

A way to generalize the diffusion equation is the following:

$$\frac{\partial^2}{\partial x^2} u(x,t) = \frac{\partial}{\partial t} u(x,t),\ x \in R,\ t \in R^+ \tag{13}$$

The above is to replace the partial derivatives in space and time with integral-differential operators that represent derivatives of a non-integer order. In this way, the fractional diffusion equation in space and time is considered as follows [96]:

$$ {}_{x}D_{\theta}^{\alpha}u(x,t) = {}_{t}^{C}D^{\beta}u(x,t), x \in R, t \in R^{+} \quad (14) $$

with α, β, and θ being the real parameters constrained by $0 < \alpha \leq 2$, $|\theta| \leq \min\{\alpha, 2-\alpha\}$, and $0 < \beta \leq 2$. In the previous equation, ${}_{x}D_{\theta}^{\alpha}$ is the fractional derivative in the Riesz–Feller space of order α and asymmetry θ, and ${}_{t}^{C}D^{\beta}$ is the fractional derivative in the Caputo time of order β [96–98].

1.6. Complex Systems (Corollary)

They have a low predictability in their macroscopic properties and in their temporal evolution; in many cases, the properties of interest follow heavy-tailed probability distributions in which the mean and sample variance are not informative. There is no characteristic scale for the occurrence of the phenomenon compared to accumulated non-extreme events, since its impact is much greater, as is the case for heat waves, climate change, pollutants' interaction with urban meteorology, urban densification, pandemics, large earthquakes, etc. Heavy-tailed phenomena are described with the power law, but probabilities such as Fréchet, Cauchy, LogNormal, etc., are useful. Validating them with empirical data is not simple: the theory indicates that these systems experience effects of a finite size, which imposes at least two domains of description on scales—large and small.

2. Materials and Methods

2.1. Study Area

The countries and locations of the measurements (T, RH, WS, PM_{10}, $PM_{2.5}$, and CO) can be viewed in Figure 6.

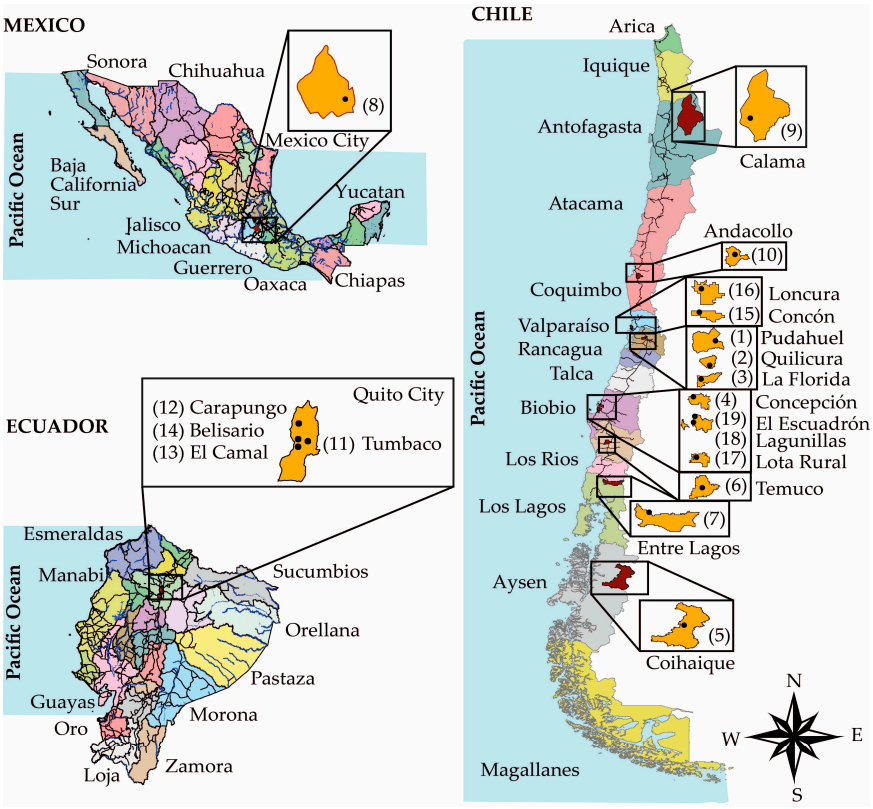


Figure 6. Distribution of monitoring stations according to the three countries used to record the measurements [43].

Table 1 specifies the height with respect to the sea level, climatology, and geography of the locations (in Mexico and Ecuador, and the others are in Chile), the measuring instruments, and the measured variables, including pollutants, magnitude of wind speed, temperature, and percentage of relative humidity.

Table 1. This table indicates the locations of the measurement instruments (some with a locality code and others not reported (NI)), the pollutants, and the meteorological variables that are measured [43,52].

Station Name	Geography	Climate	Pollution	Wind	T (°C)	RH (%)
1. Pudahuel, EMO, masl:469 (m)	Located at the bottom of the basin	Cold, dry winters and hot, dry summers.	Presence, in descending order: PM_{10}, $PM_{2.5}$, CO, SO_2, NO_2, and O_3	South–east day East–south night	15.3	57.7
2. Quilicura, EMV, masl:485(m)	Located at the bottom of the basin	Cold, dry winters and hot, dry summers.	Presence, in descending order: PM_{10}, $PM_{2.5}$, CO, SO_2, NO_2, and O_3	South–east day East–south night	22	50
3. La Florida, EML, masl:784 (m)	Andean cryonival retention mountain range and Santiago Basin	Cold, dry winters and hot, dry summers.	Presence, in descending order: PM_{10}, $PM_{2.5}$, CO, SO_2, NO_2, and O_3	South–east day East–south night	23	55
4. Kingston College, NI, masl:12 (m)	River edge plain	Cool, wet summers and cold, wet winters.	Presence, in descending order: $PM_{2.5}$, CO, PM_{10}, SO_2, NO_2, and O_3	Northwest–southeast day East–northwest night	13.3	75.2
5. Coyhaique, NI, masl:310 (m)	Inland valley plain	Cold and wet winters and summers.	Presence, in descending order: $PM_{2.5}$ and PM_{10}	Northwest–east day East–southwest night	4.8	82
6. Las Encinas, NI, masl:360 (m)	Inland valley plain	Cool, wet summers and cold, wet winters.	Presence, in descending order: PM_{10}, $PM_{2.5}$, CO, SO_2, NO_2, and O_3	West–northeast day East–west night	11.4	64.5
7. Entre Lagos, NI, masl:39 (m)	Undulating sectors of the intermediate depression	Cool, wet summers and cold, wet winters.	Presence, in descending order: $PM_{2.5}$, CO, PM_{10}, SO_2, and NO_2	East–west day West–east night	14	83
8. Mexico City, México, BJU, masl:2250 (m)	Valley bottom plain	Warm and dry in the summer and cool and wet in the winter.	Presence, in descending order: P_{M10}, $PM_{2.5}$, and CO	North–east day East–west night	16	58.8
9. Center Station, NI, masl:2400 (m)	Valley bottom plain	Cool, dry winters and mild, dry summers.	Presence, in descending order: PM_{10}, $PM_{2.5}$, CO, SO_2, NO_2, and O_3	West–northeast day East–west night	17.2	28.8
10. Andacollo, NI, masl:1017 (m)	Coastal mountain range plain	Cool, dry winters and hot, dry summers.	PM_{10}	North–southeast day East–west night	21	60

Table 1. *Cont.*

Station Name	Geography	Climate	Pollution	Wind	T (°C)	RH (%)
11. Tumbaco, Ecuador, NI, masl:2331 (m)	Cordilleran plain	Cool and wet in the winter and warm and wet in the summer.	Presence, in descending order: PM_{10}, SO_2, and O_3	Northwest–southeast day Southeast–northwest night	16	86
12. Carapungo, Ecuador, NI, masl:2851 (m)	Cordilleran valley bottom plain	Cool and wet in the winter and warm and wet in the summer.	Presence, in descending order: PM_{10}, $PM_{2.5}$, CO, SO_2, NOx, and O_3	Northwest–east day East–west night	11.3	86.1
13. El Camal Ecuador, NI, masl:2850(m)	Cordilleran valley bottom plain	Cool and wet in the winter and warm and wet in the summer.	Presence, in descending order: PM_{10}, $PM_{2.5}$, CO, SO_2, NOx, and O_3	Northwest–east day East–west night	11	87
14. Belisario Ecuador, NI, masl:2850 (m)	Cordilleran valley bottom plain	Cool and wet in the winter and warm and wet in the summer.	Presence, in descending order: PM_{10}, $PM_{2.5}$, CO, SO_2, NOx, and O_3	Northwest–east day East–west night	12	86.5
15. Concon, NI, masl:2 (m)	Sector between coastal plain and coastal mountain range	Hot, dry summers and cold, wet winters.	Presence, in descending order: PM_{10}, $PM_{2.5}$, CO, SO_2, NO_2, and O_3	West–east day East–west night	15	69.5
16. Loncura, NI, masl:3 (m)	Hill near the coast	Hot, dry summers and cold, wet winters.	Presence, in descending order: PM_{10}, $PM_{2.5}$, CO, SO_2, NO_2, and O_3	West–east day East–west night	15.1	71.5
17. Lota Rural Station, NI, masl:16 (m)	Creek and coastal hill	Cool, wet summers and cold, wet winters.	Presence, in descending order: $PM_{2.5}$, CO, PM_{10}, SO_2, NO_2, and O_3	West–east day East–west night	12.7	73.8
18. Lagunillas, NI, masl:2 (m)	Plain near the coast	Hot, dry summers and cold, wet winters.	Presence, in descending order: $PM_{2.5}$, CO, PM_{10}, SO_2, NO_2, and O_3	West–east day East–west night	14.5	68.5
19. El Escuadrón, NI, masl:2 (m)	Plain near the coast	Hot, dry summers and cold, wet winters.	Presence, in descending order: $PM_{2.5}$, CO, PM_{10}, SO_2, NO_2, and O_3	West–east day East–west night	14	68.2

2.2. The Data

The data on the pollutants and meteorological variables in this study were collected from SINCA [71], SINAICA [72], and SUIA [73] in a total of 19 locations, listed in Table 2.

Table 2. Specifications of measuring instruments. NI: no locality code information. The capital letters in the boxes of the table abbreviate the name of the equipment used (this is explained in Appendix B).

Station Name	Coordinates	PM_{10}	$PM_{2.5}$	CO	T	RH	WV	Owner
1. Pudahuel, EMO, masl:469 (m)	33°27′06.2″ S 70°40′07.8″ W	A	A	B	C	C	D	SINCA
2. Qulicura, EMV, masl:485 (m)	33°22′00″ S 70°45′00″ W	A	A	B	C	C	D	SINCA
3. La Florida, EML, masl:784 (m)	33°33′00″ S 70°34′00″ W	A	A	B	C	C	D	SINCA

Table 2. *Cont.*

Station Name	Coordinates	PM_{10}	$PM_{2.5}$	CO	T	RH	WV	Owner
4. Kingston College, NI, masl:12 (m)	36°47′4.74″ S 73°3′7.42″ W	E	E	F	G	G	H	SINCA
5. Coyhaique, NI, masl:310 (m)	45°34′44.57″ S 72°2′59.88″ W	A	A	I	J	J	K	SINCA
6. Las Encinas, NI, masl:360 [m]	38°44′55.38″ S 72°37′14.54″ W	A	A	I	L	L	L	SINCA
7. Entre Lagos, NI, masl:39 (m)	40°41′2.36″ S 72°35′47.25″ W	E	E	F	F	F	F	SINCA
8. Mexico City, BJU, Mexico, masl:2250 (m)	19°22′12.00″ N 99°9′36.00″ W	F	F	F	F	F	F	SINAICA
9. Center Station, NI, masl:2400 (m)	22°27′42.55″ S 68°55′41.45″ W	N	N	M	O	P	Q	SINCA
10. Andacollo, NI, masl:1017 (m)	30°13′39.94″ S 71°5′10.09″ W	A	----	---	R	R	S	SINCA
11. Tumbaco, NI, Ecuador, masl:2331 (m)	0°12′36″ S 78°24′00″ W,	T	T	U	V	V	D	SUIA
12. Carapungo, NI, Ecuador, masl:2851 (m)	0°5′54″ S 78°26′50″ W	T	W	B	V	V	D	SUIA
13. El Camal, NI, masl:2850 (m)	0°6′58″ S 79°26′52″ W	T	W	B	V	V	D	SUIA
14. Belisario, NI, masl:2850 (m)	0°7′57″ S 78.4°27′54″ W	T	W	B	V	V	D	SUIA
15. Concon, NI, masl:2 (m)	32°55′29.12″ S 71°30′55.73″ W	N	N	X	O	Y	Z	SINCA
16. Loncura, NI, masl:3 (m)	32°47′41.69″ S 71°29′47.11″ W	E	E	AA	P	Y	H	SINCA
17. Lota Rural Station, NI, masl:16 (m)	37° 6′0.70″ S 73° 9′7.87″ W	AB	AB	AC	G	G	AD	SINCA
18. Lagunillas, NI, masl:37 (m)	36°58′53″ S 73°9′30″ W	N	N	X	O	Y	Z	SINCA
19. El Escuadrón, NI, masl:2 (m)	36.5°57′53″ S 73.6°8.4′52″ W	N	N	X	0	Y	Z	SINCA

Missing data [43] in the time series were completed using the Kriging technique [52].

2.3. Mathematical Method Used in the Analysis of Nonlinear Time Series

Chaos theory is a basic part of nonlinear theory providing procedures to characterize dynamic systems and predict the trends of complex systems. The conceptual bases of chaos are used in physics, chemistry, biology, geology, seismology, meteorology, hydrology, etc. More specifically, chaos theory is used in the atmospheric system (a complex and nonlinear system) of our study to analyze the time series (TS) of pollutants (PM_{10}, $PM_{2.5}$, CO, NO_X, O_3, etc.) and meteorological variables (T, RH, WS, etc.) [4,50–58]. The application of chaos theory to an atmospheric system depends on phase space reconstruction theory [4].

The basic procedure in the reconstruction of a phase space is the delay method. Vectors in a new space, the embedding space, are formed with time values lagged with respect to the scalar measurements. For a delay time τ of a variable TS $X_1, X_2, \ldots, X_n$ which represents the output state of a system with n measurements, an m-dimensional phase volume (Yi) is generated as follows:

$$Y_i = \left[x_i, x_{i+\tau}, \ldots, x_{i+(m-1)\tau}\right] \quad (15)$$

with $m > 1$ and $\tau > 0$, where m is the embedding dimension. $N = n - (m - 1)\,\tau$ are the points of the reconstructed phase space vector (vectors of the embedding dimension). Equation (15) describes the evolution of the system trajectories in the m-dimensional phase space. For the sequence {Xn} of scalar measurements of the state of a dynamical system, under certain circumstances, m, with a correct delay time (τ), provides a univocal image of

the original set {Xn}, if m is large enough. The good correlation between m and τ generates a relatively stable embedding window.

According to Takens [59], τ can be chosen at random, in the absence of noise and with a data series of an infinite length. But real time series are finite and can be contaminated by noise, so, in their reconstruction process, many researches use the autocorrelation function and the correlation integral method to specify an appropriate value of τ. The autocorrelation function describes only linear correlations, while mutual information considers nonlinear distributions. The mutual information between x_i and $x_{(i+\tau)}$ weights the information in state $x_{(i+s)}$, assuming that the information in state x_i is known. By choosing m, its value does not have to be too small or large. If it is too small, attractors will not be able to adapt to the dynamics of the contaminants in the air system, which leaves the dynamics without a complete analysis. If it is very large, the extent of the data used is shortened, and then the formation of points in the phase space is reduced, probably inducing noise and interference due to the complementary dimension. Ref. [59] showed that, if $m > 2D_C + 1$, an m of the attractor can be obtained where D_C is the correlation dimension (sufficient condition). It is common to use the fraction of the false nearest neighbors (FNN) method to calculate an m that can be altered by noise in the TS data, the quantity and magnitude of the data, the sampling interval, etc. So, the results may be erroneous. Ref. [60] proposed a modified form of the FNN method that allows the chaoticity of the time series to be examined rigorously.

A chaotic system is explained by the strange attractor that forms the irregular orbits in a phase space. The specific characteristic of the strange attractor is the exponential divergence of adjacent points; chaos depends on the initial conditions (butterfly effect). The Lyapunov exponent (λ) quantitatively describes this phenomenon. If a high dependence on the initial conditions is detected in a system, it can be considered chaotic [61]. Determining the largest Lyapunov exponent (λ_L) indicates the chaotic behavior of the system. A positive Lyapunov exponent shows the divergence between neighboring trajectories [62]. For a one-dimensional dynamical system $x_{n+1} = f(x_n)$, λ is defined as follows:

$$\lambda = \lim_{n\to\infty} \ln\left(\prod_{i=1}^{n-1}\left|\frac{df(x)}{dx}\right|_{x=x_i}\right) = \lim_{n\to\infty} \ln\left(\prod_{i=0}^{n-1}\ln\left|\frac{df(x)}{dx}\right|_{x=x_i}\right) \tag{16}$$

The calculation of λ can be carried out using two methods: the Wolf method and the Jacobian method. The first is useful for the temporal variable, a noiseless series, and a small vector in an adjacent space with a highly nonlinear evolution. The second method is applied for time series with large noise and linear evolutions. In this study, λ_L is calculated considering the length n of the single variable TS $X_1, X_2, \ldots, Xn$, given the phase points $Yi = (x_i, x_{i-1}, \ldots, x_{i+(m-1)\,\tau})$. To examine the divergence in the exponential function, for the close orbits of chaotic motion, all phase points $N = n - (m - 1)\,\tau$ are selected as the reference point, and the reference phase point Yi and the reference phase point Yir, the neighbor of the nearest phase space, are the starting point of the adjacent orbits (initial condition). For time i, the orbital distance is the initial distance (Euclidean distance):

$$\delta_0^i = \|Y_i - Y_{ir}\| = \frac{1}{m}\sqrt{\sum_{k=1}^{m}\left(x_{i-(k-1)\tau} - x_{ir-(k-1)\tau}\right)^2} \tag{17}$$

Because of the exponential divergence of the nearby trajectories of the chaotic system, this is expressed as follows:

$$\delta_t = \delta_0 e^{\lambda t} \tag{18}$$

The largest Lyapunov exponent λ_L is the following:

$$\lambda_L = \frac{\ln\frac{\delta_t}{\delta_0}}{t} = \frac{\ln\delta_t}{t} - \frac{\ln\delta_0}{t} \tag{19}$$

Considering that the number of phase points is equal to N and that neighboring points undergo evolution according to t, the average of the total distance away is the following:

$$\overline{\delta}_t = \frac{1}{N}\sum_{i=1}^{N}\delta_t^i \tag{20}$$

When graphing the curve ln $\overline{\delta}_t$ against t, a straight line is drawn on the linear part of the curve, which gives the slope, which is $\lambda_{L.}$

D_C is a very important quantity to describe the geometric characteristics of the strange attractor. Its dimension may reflect the inherent complexity of urban areas, atmospheric systems, etc. D_C allows one to determine m for the reconstruction of the phase space of the TS by reporting whether the TS is generated by a dynamic process and the number of dynamic variables that can explain the atmospheric system. The most used method for this is the Grassberger and Procaccia algorithm [62]. It is based on the calculation of the correlation integral when the number of points N→∞, and, in its discrete version, it is a statistical method that can be interpreted as the number of points inside all the circles of a radius r normalized to 1, when r is big enough to include all the points without double counting. The reconstructed phase space requires one to define the distance between two phase points for the maximum weighted difference between the two vectors, as follows:

$$\left|Y_i - Y_j\right| = \max_{1\le k\le m}\left|x_{i-(k-1)\tau} - x_{j-(k-1)\tau}\right| = \left|Y_{ij}\right| = \sqrt{\sum_{k=0}^{m-1}\left(x_{i-(k-1)\tau} - x_{j-(k-1)\tau}\right)^2} \tag{21}$$

The correlation sum is that of all the related phase points and the percentage of phase points of all the possible N (N − 1)/2 [4]:

$$C(r) = \text{correlation sum} = \frac{2}{N(N-1)}\sum_{i=1}^{N}\sum_{j=i+1}^{N}\text{Heavis}\left(r - \left|Y_i - Y_{ij}\right|\right) \to C(m,r) \tag{22}$$

Heavis(x) is the unitary Heaviside function:

$$\text{Heavis}(x) = \begin{cases} 0, x \le 1 \\ 1, x > 1 \end{cases} \tag{23}$$

The definition of D_C is the following:

$$D_C = \lim_{r\to 0}\frac{\ln C(r)}{\ln r} \tag{24}$$

For values sufficiently small of r and for big quantities of data, C(r) behaves following a power law of the following kind:

$$C(r) \sim r^{D_C} \tag{25}$$

When plotting the coordinate system ln C(r) against ln r, the slope of the linear part is D_C. The correlation entropy, K_2 [4,63–66], is defined as follows:

$$K_2 = \lim_{m\to\infty}\lim_{r\to 0}\lim_{N\to\infty}\log\frac{C(m,r)}{C(m+1,r)} \tag{26}$$

where N is the number of points, m is the embedding dimension, and r is the radius of the circle or sphere. K_2 is zero, positive, or infinite for regular, chaotic, or random data, respectively. Thus, it can be stated [4] that K_2 is a lower bound of Kolmogorov's entropy, S_K (Equation (5)). That is,

$$K_2 \sim S_K \tag{27}$$

This numerical calculation is performed with software [99] that is applied to each TS (both pollutants and meteorological variables), without missing data. The chaotic analysis [4,67–69] includes the iterated function systems (IFS) fragmentation test. Symbolic dynamics allow one to calculate the Lempel–Ziv complexity (LZ > 0) referred to white noise.

The flow chart used to determine the chaotic parameters of each time series is indicated in Appendix C. Table A1 in Appendix D contains the results of the applied mathematical procedure.

2.4. The Statistics of Heavy-Tailed Distributions

They are distributions that have a higher probability of generating extreme events or outliers than a normal (Gaussian) distribution. Considering the complexity and interdependence present in internal processes (i.e., data-generating processes), they can lead to heavier tails, leading to more likely tail events and, consequently, more errors, if normal distributions are applied.

The Fréchet distribution is a special case of an extreme value distribution or heavy-tailed distribution. The distribution function that represents it is the following:

$$\Pr(X \leq x) = e^{-x^{-\beta}} \text{ and } x > 0, \beta \in (0, \infty) \quad (28)$$

where $\beta > 0$ is the shape parameter. The generalization includes a location parameter, n, and a scale parameter, $s > 0$, leaving the following:

$$\Pr(X \leq x) = e^{-\left(\frac{x-n}{s}\right)^{-\beta}}, x > n \quad (29)$$

In heavy-tailed distributions, there is a greater probability of generating extreme events compared to commonly observed distributions, such as a Gaussian or normal distribution. One of the basic concepts in heavy-tailed distributions is the behavior of the power law, such as the mean value of the squared variance of the position. Power law distributions present a scaling relationship between the probability density function and the variable of interest. In the Results Section, the calculations of the probability distribution in a basin and mountain geomorphology are presented.

3. Results

3.1. Chaotic Results

After calculating the chaotic parameters according to the procedure indicated in Appendix C and collecting the values of $C_K = S_{K,\,MET.\,VAR.}/S_{K,\,POLLUT}$, according to Table A1 of Appendix D [43,54,55,99], which incorporates six new localities, the quotient between the sum of the entropies of contaminants and that of the meteorological variables, by geographical morphologies, is presented in Table 3.

Table 3. Summary of $\Sigma\, S_k$ [bits/h]$_P$, $\Sigma\, S_k$ [bits/h]$_{MV}$, and C_K.

Morphology	masl	Localities	$\Sigma\, S_k$ [bits/h]$_P$	$\Sigma\, S_k$ [bits/h]$_{MV}$	C_K
Basin (1)	2250	México, DF (1)	1.240	0.440	0.350
Basin (2)	469	Pudahuel (2)	1.030	1.020	0.980
Basin (3)	495	Quilicura (3)	0.952	0.604	0.634
Basin (4)	784	La Florida (4)	1.006	0.679	0.675
Basin (5)	12	Kinston College (5)	0.900	0.800	0.880
Basin (6)	310	Coyhaique (6)	1.180	1.030	0.870
Basin (7)	360	Las Encinas (7)	1.200	1.170	0.970
Basin (8)	39	Entre Lagos (8)	1.780	1.740	0.970
Mountain (9)	2400	Centro Station (9)	0.760	1.230	1.600

Table 3. *Cont.*

Morphology	masl	Localities	Σ S_k [bits/h]$_P$	Σ S_k [bits/h]$_{MV}$	C_K
Mountain (10)	1017	Andacollo Station (10)	0.200	0.870	4.460
Mountain (11)	2320	Tumbaco, Ecuador (11)	1.044	1.222	1.170
Mountain (12)	2697	Carapungo, Ecuador (12)	0.844	1.182	1.400
Mountain (13)	2850	El Camal, Ecuador (13)	0.911	1.042	1.144
Mountain (14)	2850	Belisario, Ecuador (14)	0.924	1.159	1.254
Coast (15)	2	Concón Station (15)	1.010	1.260	1.240
Coast (16)	3	Loncura (16)	0.820	1.360	1.660
Coast (17)	16	Lota Rural Station (17)	0.730	0.733	1.004
Coast (18)	37	Lagunillas (18)	1.253	1.759	1.404
Coast (19)	2	El Escuadrón (19)	0.940	0.964	1.030

When graphing C_K, in Figure 7, according to the urban settlements in the three geographical morphologies of this study—basin, mountain, and coast—these were numbered by (1), (2) . . . (19) [43,55,99].

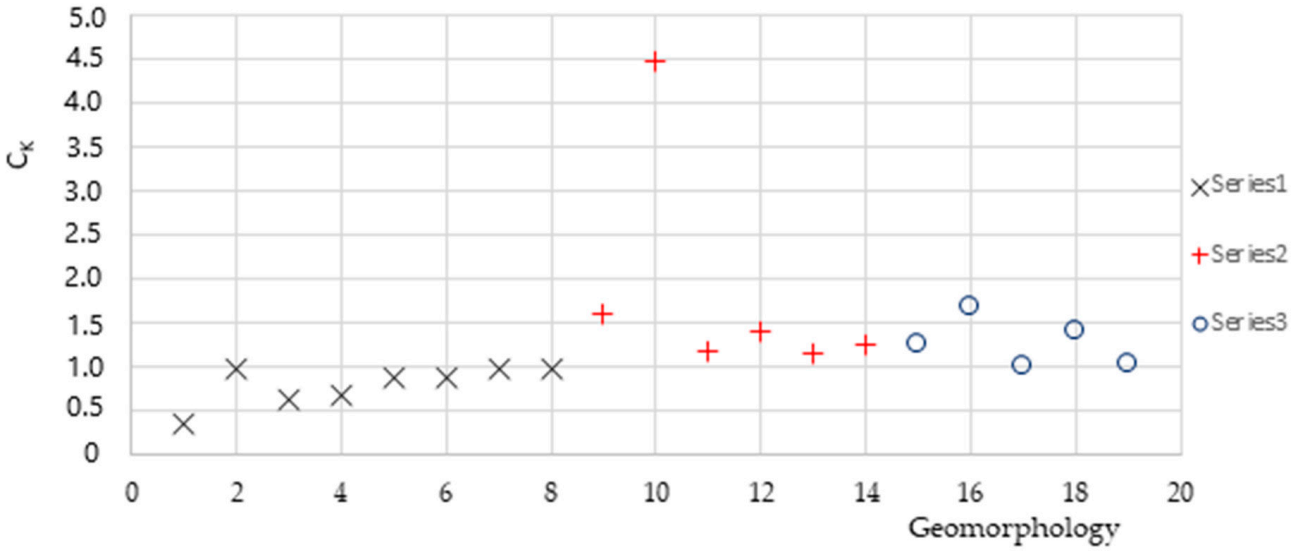


Figure 7. C_K for cities in basin (Series 1), mountain (Series 2), and coast (Series 3).

Table 4 summarizes data from Table A1 of Appendix D. In its columns it considers the geomorphology, the measurement period, the loss of information according to the pollutants (P) and meteorological variables (MV), the quotient between the loss of information of MV and P, the comparative loss of information ($<\Delta I>_{comp}$), the comparative persistence (H_{comp}), and the fractal dimension for P and MV. Equation (2) represents the relationship between the fractal dimension (D_F) and the Hurst exponent (H). H is used as a measure of long-range dependence within a time series (the past influences the future or the persistence) and quantifies the relative tendency of a time series to regress strongly to the mean or cluster in one direction. A value of H in the range 0.5–1, as it was the case for this study (Table A1, Appendix D), indicates a time series with a long-term positive autocorrelation, meaning that a high (or low) value in the series will probably be followed by another high (or low) value and that values in the future will also tend to be high (or low).

Table 4. This table shows the loss of information on P, $\Sigma(<\Delta I>)_P$, and on MV, $\Sigma(<\Delta I>)_{MV}$, according to the localities. The fifth column is the quotient between the loss of information from MV and that of P. The numbers in the sixth and seventh columns indicate the following: (1) P lose information slower and are more stable than MV; (2) MV lose information slower and are more stable than P; (3) P are more persistent (ability to influence the future) than MV; and (4) MV are more persistent than P. The eighth and ninth columns provide the value of the fractal dimension of P and MV.

	Period	$\Sigma(<\Delta I>)_P$	$\Sigma(<\Delta I>)_{MV}$	$<\Delta I>_{MV}/<\Delta I>_P$	$<\Delta I>_{comp}$	H_{comp}	D_{FP}	D_{FMV}
Basin								
Pudahuel	2018/2019	−2.89	−5.07	1.75	(2)	(3)	1.069	1.080
Quilicura	2019/2022	−4.63	−3.17	0.68	(1)	(3)	1.037	1.022
La Florida	2019/2022	−3.29	−2.23	0.67	(1)	(3)	1.034	1.015
Kingst. Coll	2017/2018	−2.06	−6.45	3.13	(2)	(3)	1.094	1.100
Coyhaique	2016/2017	−5.88	−3.51	0.60	(1)	(3)	1.094	1.126
Las Enc. Stat	2018	−3.00	−8.75	2.92	(2)	(3)	1.089	1.111
Ent. Lag. Stat	2011	−8.25	−9.50	1.15	(2)	(4)	1.199	1.119
Mex. City	2018	−1.80	−4.50	2.50	(2)	(4)	1.073	1.024
Mountain								
Centro Stat	2016/2017	−3.50	−3.94	1.13	(2)	(3)	1.088	1.095
Tumbaco	2020/2021	−6.64	−2.59	0.40	(1)	(4)	1.124	1.065
Carapungo	2020/2021	−6.26	−2.74	0.44	(1)	(4)	1.110	1.064
Andac. Stat	2016/2019	−0.56	−3.97	7.09	(2)	(4)	1.094	1.071
El Camal	2013/2017	−5.43	−0.840	0.16	(1)	(4)	1.070	1.063
Belisario	2013/2017	−5.28	−1.043	0.20	(1)	(4)	1.073	1.064
Coast								
Con-Con Stat	2018/2019	−1.85	−5.67	3.07	(2)	(3)	1.064	1.109
Loncura Stat	2016/2017	−3.37	−4.72	1.40	(2)	(4)	1.117	1.070
Lot. Ru Stat	2016/2017	−3.00	−1.97	0.66	(1)	(4)	1.108	1.102
Lagunillas	2021/2023	−3.55	−4.03	1.14	(2)	(4)	1.075	1.071
El Escuadron	2021/2023	−5.15	−5.01	0.97	(1)	(4)	1.083	1.083

According to Appendix E, using a first approximation treatment and the Lyapunov relation, we can obtain $< x^2 > \sim t^{\frac{S_{K,MV}}{S_{K,P}}}$. If it is assumed that $t^{\frac{S_{K,MV}}{S_{K,P}}} \to t^{\alpha}$, where α is the exponent of the temporal variable for anormal diffusion processes and would be similar to $\alpha = \frac{S_{K,MV}}{S_{K,P}}$ considered from a phenomenological point of view, then the following are true:

(1) C_K can be used, in a first approximation criterion, as a discriminant of the dominant effect of pollutants on local meteorology and its diffusion according to cities located as per the equation below.

$$\alpha = C_K = \frac{S_{K,MET.VAR}}{S_{K,POLLUT}} = \begin{cases} < 1, \text{ case1} & \text{basin} \\ > 1, \text{ case 2} & \text{high mountain} \\ > 1, \text{ case 3} & \text{coast} \end{cases}, \quad (30)$$

(2) The comparison of whether D_{FP} is greater with respect to D_{FMV} according to the total number of localities of each geomorphology type indicates that this is the case in 4/8 basins (there is a certain balance in the localities), 5/6 mountains, and 4/5 coasts. On the coast and mountain range, the fractality of the phase space of the pollutants needs more dimension to be able to expand to finer and finer scales, which can favor its diffusion through meteorology.

(3) The basin shows the greatest persistence in pollutants (subdiffusion), and the coast and mountains show the greatest persistence in the meteorological variables that promote superdiffusion.

3.2. Heavy Tail Probability

The Fréchet distribution is applied to three geomorphologies: basin, mountain, and coast.

3.2.1. Basin

Our study considered the case of six monitoring stations in a basin geomorphology in the location of Santiago de Chile. The data were extracted from [50], a more independent source, and are summarized in Table 5. After calculating the Kolmogorov entropy, C_K was constructed for the six locations and used as the domain of the Fréchet distribution function, $C_K \in (0, \infty)$.

Table 5. Santiago, Chile, comparative table entropies $S_{K,\,HR}/S_{K,\,P}$, in the periods of 2010/2013, 2017/20230, and 2019/2022 (six neighboring communes).

	2010–2013	**2017–2020**	**2019–2022**
Station	C_K	C_K	C_K
EML (La Florida)	0.86511025	0.81420419	0.6749503
EMM (Las Condes)	0.93677419	0.85704125	0.68085106
EMO (Pudahuel)	0.9892562	0.60920245	0.59803044
EMS (Puente Alto)	0.93609296	0.73443008	0.58932039
EMV (Quilicura)	0.83997205	0.8147541	0.63445378
EMN (Santiago—Parque O'Higgins)	0.82429784	0.77417174	0.5350488

Figure 8 shows the evolution of the heavy tail probability in the three periods of 2010/2013, 2017/2020, and 2019/2022.

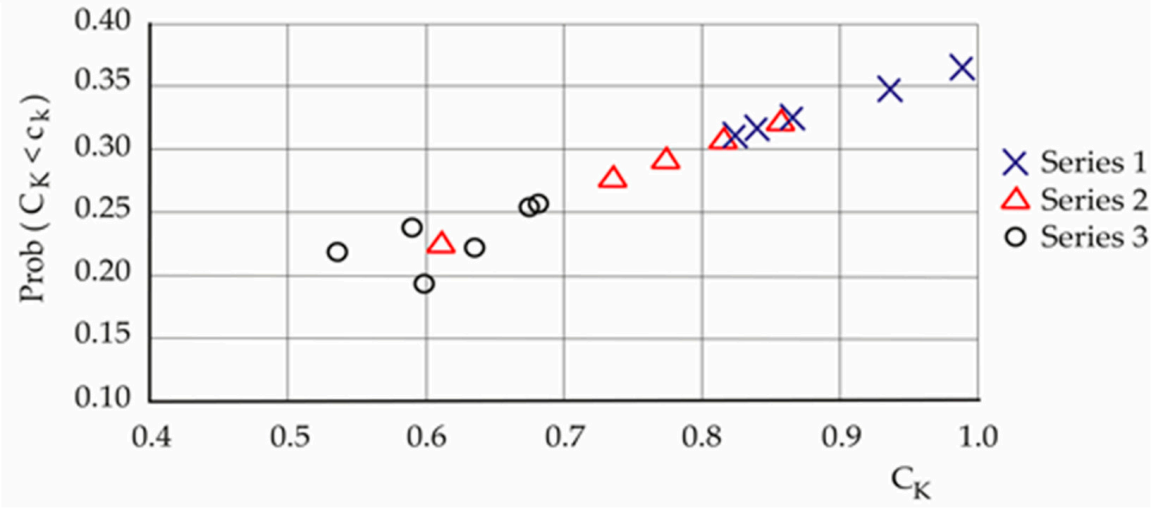


Figure 8. Probability of a heavy tail for each monitoring station according to the study periods. x: 2010/2013; Δ: 2017/2020; and o: 2019/2022.

The greatest influence of urban meteorology on climatology occurred in the period of 2010/2013 (x), decreased in 2017/2020 (Δ), and decreased further in the period of 2019/2022 (o), as shown by the heavy-tailed distribution of Fréchet when considering the increase and interdependence between pollutants, urban densification, demographic increase, heat waves, high-rise construction, persistent drought, etc. These phenomena are very complex and correlated, and their presence dates back decades. The Santiago de Chile basin has a permanent and increasing level of pollution, which causes a subdiffusive polluting regime, as indicated by Equation (30). It is highlighted that, in part of the 2019/2022 period (2020–mid-2022) the coronavirus pandemic occurred, causing human activity to decline, so there was less contamination, which is reflected in the distribution of the data (o) in Figure 8. The average probability of the three periods, in Table 6, shows the influence of urban meteorology on the pollutants, and its general average is of the order of 28.6%.

Table 6. Heavy tail probability averaged in each study period.

Period	Prob
2010/2013	34%
2017/2020	29%
2019/2022	23%

3.2.2. Mountain

In our study, four stations were considered to be located in a mountain geomorphology (Ecuador), listed in Table A1 of Appendix D. After calculating the Kolmogorov entropy, C_K was constructed for the four locations, as shown in Table 7, and was used as the domain of the function of the Fréchet distribution, $C_K \in (0, \infty)$.

Table 7. Periods of data recording, locations, C_K value, and heavy tail probability.

Period	masl (m)	Location	$S_{K,P}$	$S_{K,MV}$	C_K	Prob	Symbol
2021/2022	2320	Tumbaco, Ecuador (11)	1.044	1.222	1.170	0.41396870	o
2021/2022	2697	Carapungo, Ecuador (12)	0.844	1.182	1.400	0.46579605	◊
2013/2017	2850	El Camal, Ecuador (13)	0.911	1.042	1.144	0.40739806	Δ
2013/2017	2850	Belisario, Ecuador (14)	0.924	1.159	1.254	0.43414516	□

Figure 9 shows the distribution of a heavy tail according to different periods of data recording in the four high mountain localities in Ecuador.

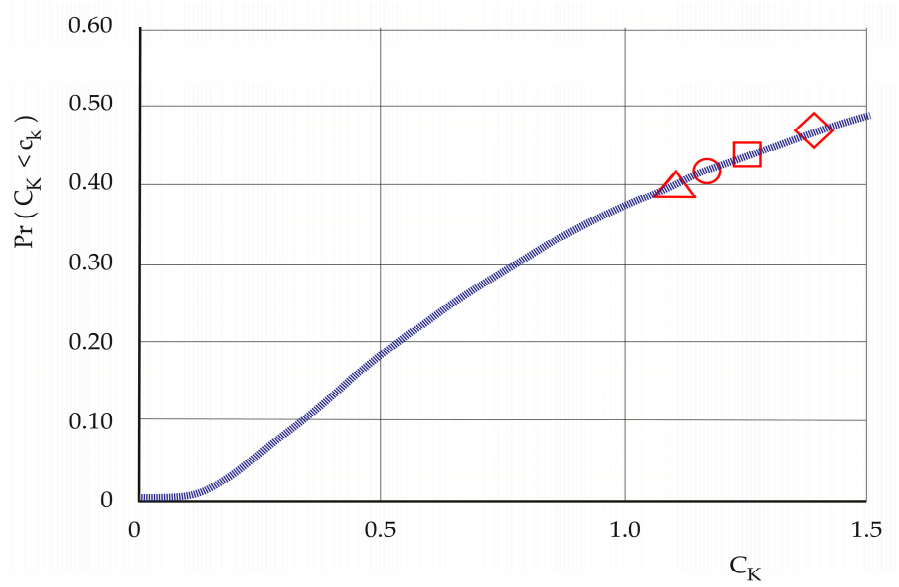


Figure 9. Heavy-tailed probability distribution, accounting for the influence of meteorology on pollutants.

This probability shows that the dominance over mountain diffusion processes, regardless of the measurement period, is exerted by urban meteorology in a stable manner, of the order of 43% on average, well-above the value for the basin geomorphology (28, 6%).

3.2.3. Coast

Three stations (relatively neighboring) were considered to be located in a coast geomorphology (Chile), as listed in Table A1 of Appendix D. After calculating the Kolmogorov entropy, C_K was constructed for the three locations, shown in Table 8, and was used as the domain of the function of the Fréchet distribution, $C_K \in (0, \infty)$.

Table 8. Periods of data recording, locations (on the coast of Chile), C_K value, and heavy tail probability.

Period	masl (m)	Location	C_K	Prob	Symbol
2018/2019	2	Concón Station (15)	1.240	0.43088926	Δ
2016/2017	3	Loncura (16)	1.660	0.51341334	◊
2021/2023	37	Lagunillas (18)	1.404	0.46579605	□

Figure 10 shows the distribution of a heavy tail according to different periods of data recording in the three coast localities (relatively neighboring) in Chile.

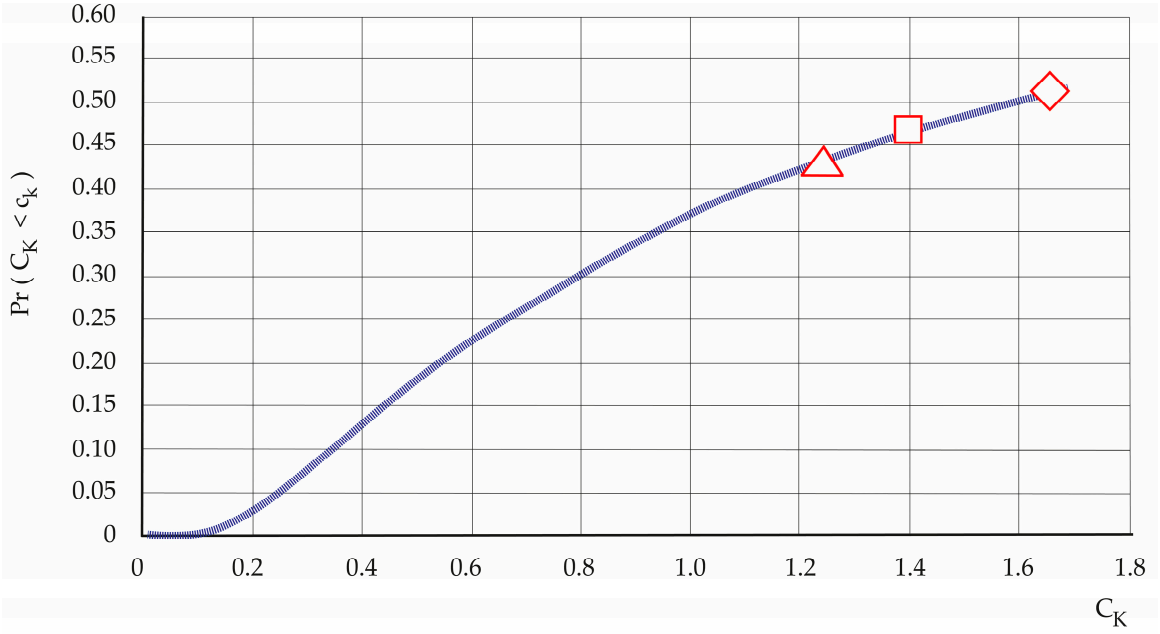


Figure 10. Heavy-tailed probability distribution accounting for the influence of meteorology on pollutants.

The probability shows that the dominance over coast diffusion processes, regardless of the measurement period, is exerted by urban meteorology in a stable manner, of the order of 47% on average, well-above the value of the basin geomorphology (28, 6%).

4. Discussion

Diffusion is related to the concept of entropy. Entropy is a measure of the disorder or randomness of a system. In the context of diffusion, the entropy of a system tends to increase as the particles of a substance become more evenly distributed throughout the system. This is because the diffusion process leads to a more random distribution of particles, which is associated with an increase in disorder or randomness. For example, if we consider a container full of gas, the gas is initially concentrated in one part of the container, and the entropy of the system is low. However, as the gas diffuses and spreads to fill the entire volume of the container, the entropy of the system increases, because the gas particles are now more evenly distributed. Anomalous diffusions appear in disordered systems or systems that are far from a thermodynamic equilibrium, where the heterogeneities of the system induce an anomalous behavior in the average square displacement of a particle which diffuses in that medium, and its displacement is conditioned by the other systems.

Diffusion in fractal media is a form of random motion that is characterized by long-term memory and persistent fluctuations. The Hurst exponent, H, measures the smoothness of a time series. If $0.5 < H < 1$, they are called Levy flights. $H > 0.5$ implies persistence

(positive correlation), where the trajectory tends to continue in the current direction and, thus, produces enhanced or anomalous diffusion [4].

Levy flights are a type of random walk whose increments are distributed according to a heavy-tailed probability distribution [96–98]. Heavy-tailed distributions are probability distributions that have thick tails, meaning that they have a higher probability of extreme values than other distributions. In this case, diffusion is a type of random walk that is characterized by the property of memory: the next step in the random walk depends on the previous step. This means that the current step is more likely to be comparable to the previous step than to be different from it. These distributions can be used to model real-world phenomena such as atmospheric pollutant diffusion processes, as pollutants tend to move in the same direction over long periods of time.

In a basin morphology, the diffusion of contaminants is low, being one of the most serious problems which this geography presents for the health of its population. In this morphology, urban meteorology does not favor the diffusion of polluting materials, and we can speak of subdiffusion, that is, $\alpha < 1$, which is compatible with the value, of less than 1, of quotient C_K.

The direct observation of mountain and coastal geomorphologies reveals an environment that is not much contaminated. From the perspective of urban meteorology and the calculation of $\Sigma\ S_k\ [bits/h]_{MV}$, it is greater than the value of the sum of $\Sigma\ S_k\ [bits/h]_P$ (PM_{10}, $PM_{2.5}$, CO), which determines that C_K is greater than 1. For an anomalous diffusion, it corresponds to $\alpha > 1$, which describes a case of superdiffusion.

It is well established that diffusion processes that take place in fractal and/or random media generally present subdiffusive and superdiffusive behaviors induced by the mean geometry and associated to strong correlations in the motion of the particles [93,100,101].

From Table 4, the below can be concluded.

Basin: according to the measurements from recent years, pollution has become more dominant. In the case of Coyhaique city, for decades the population has used firewood and charcoal, which has determined its high level of pollutants. The persistence, that is, the capacity to influence the future, of pollution is dominant towards the most current period. The entropy of the system of meteorological variables is lower, so the capacity for the expansion of nearby trajectories towards new regions of the spatial state decreases, meaning that the system is less diffusive. The configuration of a basin is like a semi-closed or semi-confined system (finite volume), where there is a geometric barrier (approximately a positive paraboloid) which acts as an obstacle, which can limit the influence of the meteorological system. This barrier can be interpreted as a mechanical asymptote that moderates the entropy of meteorology.

Mountain: Pollutants lose information slower, depending on the measurement period, but meteorology is more persistent. The entropy of meteorology is greater than that of pollutants.

Coast: Meteorological variables lose information slower than pollutants. In the town of Con-Con, there is a refinery, and Lota Rural Station (Lot. Ru Stat) is close to a mine that exploited coal (which closed a few years ago). In this geomorphology, it also happens that, in general, the entropy of meteorology is greater than that of pollutants.

When comparing whether D_{FP} is greater with respect to D_{FMV} according to the localities of each geomorphology, it is found that, in the basin type, it is higher in four of the eight locations (there is a certain balance in the localities), in the mountain type, in five of the six locations, and, in the coast, in four of the five locations. These results can be interpreted to indicate that the fractal dimension for the pollutants, in the majority of the coastal and mountainous locations studied, is an exponent that requires a phase space of a greater dimension to fill it completely while expanding towards increasingly finer scales, which does not happen with most meteorological variables.

The heavy-tailed statistic corresponds to the definition of C_K and the expression for diffusion $t^{\frac{S_{K,MV}}{S_{K,P}}} \rightarrow t^{\alpha}$ according to geomorphology, indicating who has the greatest probability of influencing the anomalous diffusion processes—urban meteorology or pollutants.

5. Conclusions

The time series of urban meteorology (temperature, relative humidity, and wind speed magnitude) and atmospheric pollutants (PM_{10}, $PM_{2.5}$, and CO) were studied, in different time periods, in three different geomorphologies: basin, mountain, and coast. It was shown that all the time series were chaotic, including the Lyapunov exponent ($\lambda > 0$), the correlation dimension ($D_C < 5$), the Kolmogorov entropy ($S_K > 0$), the Hurst exponent ($0.5 < H < 1$), the Lempel–Ziv complexity ($LZ > 0$), the loss of information ($<\Delta I> < 0$), using the Lyapunov exponent, and the existence of a fractal dimension (D).

Through the C_K parameter, defined as the quotient between the entropies of urban meteorology and the entropies of the pollutants, it was verified that, in a basin morphology, its value is less than 1, as the entropy of the pollutants is greater than that of the meteorological variables. A quotient of less than 1 explains that, in a morphology with these characteristics, the diffusion of contaminants is not favored, which is a case of anomalous subdiffusion. On the contrary, in the geomorphologies of a coast and a mountain range, the entropy of urban meteorology is greater, causing C_K to be greater, which favors anomalous superdiffusion. The heavy tail probability confirms these findings.

Author Contributions: Conceptualization, P.P.; methodology, P.P.; software, P.P. and E.M.; validation, P.P., C.P., G.N. and E.M.; formal analysis, P.P.; investigation, P.P.; resources, P.P.; data curation, P.P., E.M. and G.N.; writing—original draft preparation, P.P., G.N. and E.M.; writing—review and editing, P.P., C.P., G.N. and E.M.; visualization, C.P., G.N. and E.M.; supervision, P.P.; project administration, P.P.; funding acquisition, P.P. All authors have read and agreed to the published version of the manuscript.

Funding: This research was supported by ANID/CONICYT/FONDECYT Regular 1240127.

Data Availability Statement: The data were obtained from the public network for the online monitoring of air pollutant concentration and meteorological variables in Chile. This network is distributed throughout Chile, without access restrictions, and is the responsibility of the SINCA, the National Air Quality Information System, dependent on the Environment Ministry of Chile [71]. The data for the two study periods will be available for free use on the following page: https://sinca.mma.gob.cl (accessed on 13 April 2023). In México [72], we used data from the Sistema Nacional de Información Ambiental y de Recursos Naturales de México. The data for the study period will be available for free use on the following page: https://www.gob.mx/semarnat/acciones-y-programas/sistema-nacional-de-informacion-ambiental-y-de-recursos-naturales (accessed on 12 February 2023). In Ecuador [73], we referred to the Secretaria de Ambiente del Municipio del Distrito Metropolitano de Quito. The data for the study period will be available for free use on the web page http://www.quitoambiente.gob.ec/index.php/carapungo (accessed on 14 January 2023).

Acknowledgments: To the Research Directorate of the Universidad Tecnológica Metropolitana (UTEM) that made possible the progress of this study and to the Department of Physics of the UTEM for their collaboration.

Conflicts of Interest: The authors declare no conflicts of interest. The funders had no role in the design of the study; in the collection, analyses, or interpretation of data; in the writing of the manuscript; or in the decision to publish the results.

Appendix A

The linear diffusion in time is calculated as follows:

$$< x^2 >= \int_{-\infty}^{+\infty} \left(x - \dot{x}\right)^2 \frac{1}{\sqrt{4\pi Dt}} e^{-\frac{x^2}{4Dt}} dx = \text{variance}, \tag{A1}$$

Using changing variables, $v = x - \dot{x} \rightarrow x = v + \dot{x} \rightarrow dx = dv$.

$$< x^2 >= \int_{-\infty}^{+\infty} (v)^2 \frac{1}{\sqrt{4\pi Dt}} e^{-\frac{(v+\dot{x})^2}{4Dt}} dv = 2\int_{0}^{+\infty} (v)^2 \frac{1}{\sqrt{4\pi Dt}} e^{-\frac{(v+\dot{x})^2}{4Dt}} dv = 2\frac{1}{\sqrt{4\pi Dt}} \frac{\sqrt{\pi}\left(\sqrt{4Dt}\right)^3 (2-1)!!}{2^{1+1}} \tag{A2}$$

The average square displacement traveled by the diffusing substance grows linearly with time (Einstein):

$$< x^2 >= 2Dt \quad \text{(A3)}$$

Appendix B

Abbreviations

A: Attenuation Beta-Met One 1020; B: Gas Correlation Filter IR Photometry-Thermo 48i; C: Vaisala HMP35A; D: Sensor—Met One 010C; E: method based on the principle of beta attenuation; F: US EPA equivalent; G: polynomial sensor; H: magnetic coil type; I: IR Photometry−Teledyne T300; J: Sensor Lastem DMA875; K: Sensor Lastem DNA802; L: Sensor−LSI Lastem DMA675; N: continuous and discrete gravimetric; M: continuous infrared light absorption; O: RTD resistance; P: thermistor; Q: anemometer with three-cups vector; R: Sensor−CS HMP50; S: Sensor−RM Young 530; T: Thermo Scientific/FH62C14; U: Thermo/146C/146i; V: Thies Clima; W: Thermo Andersen/FH62C14; X: non-dispersive infrared photometry; Y: capacitive measurement technique; Z: sinusoidal signal with frequency proportional to wind speed; AA: non-dispersive infrared with correlation filter; AB: laser spectrometry; AC: IRND with correlation gas filter; and AD: pulse generation

Appendix C

Flowchart

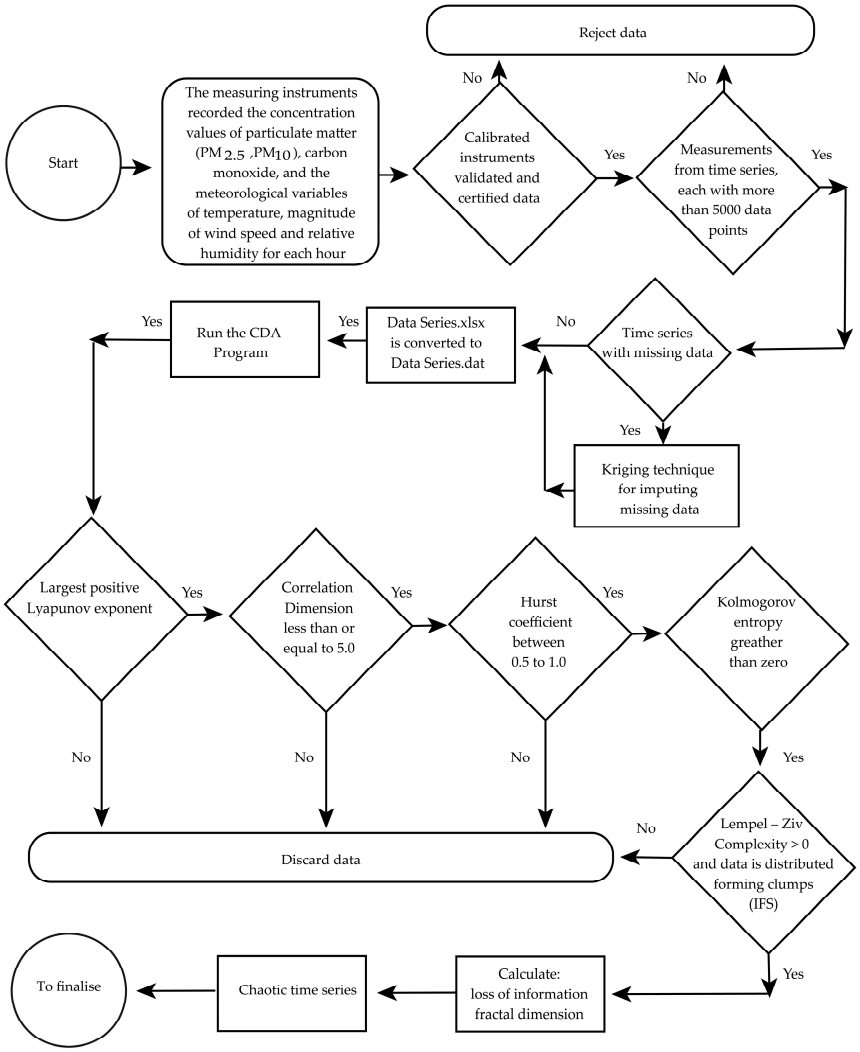


Figure A1. Figure shows the procedure followed in the chaotic study of each time series [63].

Appendix D

Table A1. Numerical values of the parameters for a total of 2,144,658 data points: Lyapunov exponent (λ), correlation dimension (D_C), Kolmogorov entropy (S_K), Hurst exponent (H), Lempel–Ziv complexity (LZ), and loss of information (<ΔI>).

Basin	Variables Each 17,520 h	λ [bits]	Dc	S_k [bits/h]	H	LZ	<ΔI>
(a). Pudahuel (2018–2019, 584 masl)	CO	0.017 ± 0.006	2.937 ± 0.115	0.459	0.933	0.014	−0.056
	PM_{10}	0.593 ± 0.030	3.531 ± 1.665	0.246	0.942	0.178	−1.970
	$PM_{2.5}$	0.260 ± 0.026	1.231 ± 0.309	0.326	0.919	0.309	−0.864
					0.931		−0.963
	T	0.261 ± 0.016	2.551 ± 0.069	0.289	0.917	0.238	−0.867
	WS	0.960 ± 0.018	4.029 ± 0.292	0.371	0.908	0.468	−3.189
	RH	0.305 ± 0.021	3.026 ± 0.119	0.355	0.936	0.449	−1.013
					0.920		−1.690
	Variables each 17,520 h						
(b) Kingston College (2017–2018, 2 masl)	CO	0.141 ± 0.012	2.240 ± 0.058	0.389	0.915	0.076	−0.468
	PM_{10}	0.224 ± 0.027	1.412 ± 0.183	0.179	0.908	0.204	−0.744
	$PM_{2.5}$	0.255 ± 0.025	2.435 ± 1.032	0.334	0.896	0.523	−0.847
					0.906		−0.686
	T	0.269 ± 0.017	1.879 ± 0.082	0.292	0.915	0.200	−0.894
	WS	0.613 ± 0.018	4.749 ± 0.647	0.342	0.892	0.569	−2.036
	RH	1.060 ± 0.023	2.040 ± 0.327	0.161	0.893	0.595	−3.521
					0.900		−2.150
	Variables each 28,463 h						
(c). Quilicura (2019–2022, 485 masl)	CO	0.580 ± 0.077	2.127 ± 0.110	0.285	0.933	0.0014	−1.927
	PM_{10}	0.574 ± 0.030	0.945 ± 0.017	0.252	0.930	0.175	−1.907
	$PM_{2.5}$	0.241 ± 0.021	1.432 ± 0.216	0.415	0.938	0.337	−0.800
					0.934		1.545
	T	0.161 ± 0.014	1.559 ± 0.761	0.153	0.920	0.054	−0.535
	WS	0.080 ± 0.013	1.939 ± 0.078	0.351	0.940	0.165	−0.266
	RH	0.714 ± 0.048	2.704 ± 0.036	0.100	0.934	0.027	−2.372
					0.931		−1.058
	Variables each 28,463 h						
(d). La Florida 2019–2022, 784 masl)	CO	0.025 ± 0.007	2.089 ± 0.052	0.382	0.933	0.016	−0.083
	PM_{10}	0.716 ± 0.031	1.067 ± 0.203	0.257	0.930	0.164	−2.378
	$PM_{2.5}$	0.246 ± 0.020	1.306 ± 0.172	0.367	0.946	0.257	−0.817
					0.936		−1.093
	T	0.191 ± 0.016	1.632 ± 0.798	0.175	0.920	0.073	−0.634
	WS	0.314 ± 0.016	1.991 ± 0.045	0.275	0.942	0.181	−1.043
	RH	0.167 ± 0.017	2.465 ± 0.701	0.229	0.934	0.144	−0.555
					0.932		−0.744
	Variables each 17,520 h						
(e). Coyhaique (2016–2017, 310 masl)	CO	0.740 ± 0.026	3.765 ± 1.356	0.207	0.867	0.477	−2.458
	PM_{10}	0.500 ± 0.031	1.523 ± 0.996	0.656	0.926	0.236	−1.661
	$PM_{2.5}$	0.531 ± 0.032	1.960 ± 0.737	0.312	0.925	0.256	−1.764
					0.906		−1.961
	T	0.718 ± 0.033	1.660 ± 0.605	0.436	0.903	0.486	−2.385
	WS	0.331 ± 0.025	3.750 ± 0.975	0.211	0.816	0.364	−1.100
	RH	0.007 ± 0.005	1.660 ± 0.605	0.383	0.903	0.007	−0.023
					0.874		1.169

Table A1. *Cont.*

Basin	Variables Each 17,520 h	λ [bits]	Dc	S_k [bits/h]	H	LZ	<ΔI>
	Variables each 8760 h						
(f). Las Encinas Station (2018, 360 masl)	CO	0.016 ± 0.008	1.107 ± 0.025	0.197	0.928	0.015	−0.053
	PM_{10}	0.146 ± 0.034	0.990 ± 0.031	0.218	0.909	0.307	−0.485
	$PM_{2.5}$	0.728 ± 0.053	3.108 ± 0.847	0.784	0.897	0.422	−2.418
					0.911		−0.985
	T	0.477 ± 0.023	2.823 ± 0.214	0.467	0.909	0.365	−1.585
	WS	1.335 ± 0.039	1.138 ± 0.120	0.388	0.862	0.449	−4.435
	RH	0.823 ± 0.034	0.792 ± 0.113	0.317	0.897	0.308	−2.734
					0.889		−2.918
	Variables each 8760 h						
(g). Entre Lagos Station (2011, 39 masl)	CO	1.090 ± 0.093	1.678 ± 0.269	0.626	0.854	0.353	−3.621
	PM_{10}	0.586 ± 0.074	0.988 ± 0.611	0.624	0.767	0.587	−1.947
	$PM_{2.5}$	0.808 ± 0.082	1.025 ± 0.210	0.531	0.783	0.644	−2.684
					0.801		−2.751
	T	1.166 ± 0.087	1.110 ± 0.233	0.913	0.847	0.388	−3.873
	WS	1.166 ± 0.096	2.158 ± 0.228	0.448	0.838	0.353	−3.873
	RH	0.527 ± 0.065	2.151 ± 0.105	0.379	0.958	0.400	−1.751
					0.881		−3.166
	Variables each 17,520 h						
(h). México City (2018, 2250 masl)	CO	0.248 ± 0.025	2.602 ± 0.591	0.374	0.932	0.138	−0.824
	PM_{10}	0.160 ± 0.039	1.112 ± 0.147	0.409	0.905	0.287	−0.532
	$PM_{2.5}$	0.135 ± 0.030	1.107 ± 0.09	0.456	0.949	0.350	−0.448
					0.927		−0.601
	T	0.803 ± 0.041	1.386 ± 0.794	0.083	0.998	0.283	−2.668
	WS	0.532 ± 0.037	4.145 ± 0.154	0.190	0.933	0.211	−1.767
	RH	0.019 ± 0.009	2.279 ± 0.511	0.164	0.999	0.006	−0.063
					0.976		−1.499
Mountain	Variables each 17,520 h						
(i). Center Station (2016–2017, 2400 masl)	CO	0.681 ± 0.018	4.316 ± 2.747	0.058	0.919	0.397	−2.262
	PM_{10}	0.071 ± 0.014	2.802 ± 1.566	0.197	0.919	0.088	−0.236
	$PM_{2.5}$	0.301 ± 0.021	4.067 ± 0.086	0.509	0.898	0.463	−1.000
					0.912		−1.166
	T	0.318 ± 0.016	3.143 ± 0.086	0.298	0.913	0.266	−1.056
	WS	0.694 ± 0.037	4.180 ± 0.26	0.497	0.882	0.565	−2.305
	RH	0.175 ± 0.012	3.016 ± 0.096	0.431	0.921	0.423	−0.581
					0.905		−1.314
	Variables each 9468 h						
(j). Tumbaco, Ecuador (2020 −2021, 2320 masl)	CO	0.631 ± 0.098	1.929 ± 0.079	0.183	0.929	0.006	−2.096
	PM_{10}	0.493 ± 0.035	1.292 ± 0.130	0.425	0.809	0.044	−1.637
	$PM_{2.5}$	0.874 ± 0.040	2.164 ± 0.636	0.436	0.892	0.044	−2.903
					0.876		−2.212
	T	0.033 ± 0.009	4.229 ± 0.085	0.498	0.928	0.002	−0.110
	WS	0.586 ± 0.086	3.719 ± 0.063	0.345	0.929	0.002	−1.946
	RH	0.160 ± 0.017	1.731 ± 0.218	0.379	0.948	0.149	−0.531
					0.935		−0.862

Table A1. *Cont.*

Basin	Variables Each 17,520 h	λ [bits]	Dc	S_k [bits/h]	H	LZ	<ΔI>
	Variables each 11,000 h						
(k). Carapungo, Ecuador (2020 −2021, 2697 masl)	CO	0.695 ± 0.091	3.348 ± 0.199	0.296	0.930	0.002	−2.308
	PM_{10}	0.296 ± 0.024	1.188 ± 0.076	0.273	0.843	0.050	−0983
	$PM_{2.5}$	0.893 ± 0.037	1.720 ± 0.390	0.275	0.897	0.050	−2.966
					0.890		−2.086
	T	0.077 ± 0.010	4.259 ± 0.097	0.499	0.930	0.002	−0.256
	WS	0.610 ± 0.082	3.670 ± 0.048	0.389	0.930	0.002	−2.026
	RH	0.137 ± 0.015	1.545 ± 0.132	0.294	0.947	0.142	−0.455
					0.936		−0.912
	Variables each 29,998 h						
(l). Andacollo Station (2016–2019, 1017 masl)	CO						
	PM_{10}	0.167 ± 0.020	4.477 ± 0.541	0.195	0.906	0.110	−0.555
	$PM_{2.5}$						
					0.906		−0.555
	T	0.499 ± 0.021	1.928 ± 0.439	0.419	0.917	0.304	−1.658
	WS	0.670 ± 0.022	3.000 ± 0.968	0.306	0.895	0.380	−2.226
	RH	0.027 ± 0.007	2.514 ± 0.05	0.146	0.974	0.113	−0.090
					0.929		−1.325
	Variables each 29,998 h						
(ll). Camal, Ecuador (2013 −2017, 2850 masl)	CO	0.037 ± 0.008	2.551 ± 0.214	0.407	0.933	0.024	−0.123
	PM_{10}	0.745 ± 0.031	4.037 ± 0.686	0.191	0.936	0.254	−2.475
	$PM_{2.5}$	0.853 ± 0.031	1.284 ± 0.193	0.313	0.921	0.226	−2.833
					0.930		−1.810
	T	0.096 ± 0.013	4.678 ± 0.105	0.410	0.933	0.043	−0.319
	WS	0.091 ± 0.013	3.424 ± 0.059	0.272	0.934	0.047	−0.302
	RH	0.065 ± 0.012	2.003 ± 0.266	0.360	0.940	0.095	−0.216
					0.936		−0.279
	Variables each 29,998 h						
(m). Belisario, Ecuador (2013–2017, 2850 masl)	CO	0.021 ± 0.007	2.485 ± 0.151	0.341	0.933	0.022	−0.069
	PM_{10}	0.725 ± 0.032	2.932 ± 0.514	0.313	0.937	0.246	−2.408
	$PM_{2.5}$	0.844 ± 0.032	1.362 ± 0.259	0.270	0.910	0.085	−2.804
					0.926		−1760
	T	0.151 ± 0.015	4.674 ± 0.107	0.420	0.932	0.043	−0.502
	WS	0.095 ± 0.013	4.490 ± 0.077	0.381	0.934	0.047	−0.316
	RH	0.068 ± 0.012	2.084 ± 0.377	0.358	0.943	0.095	−0.226
					0.936		−0.348
Coast	Variables each 17,520 h						
(n). Concón Station (2018–2019, 2 masl)	CO	0.023 ± 0.010	2.457 ± 0.414	0.326	0.927	0.016	−0.076
	PM_{10}	0.058 ± 0.024	0.861 ± 0.053	0.211	0.892	0.067	−0.193
	$PM_{2.5}$	0.475 ± 0.046	1.178 ± 0.271	0.474	0.989	0.166	−1.578
					0.936		−0.616
	T	0.105 ± 0.018	1.462 ± 0.995	0.140	0.920	0.094	−0.349
	WS	0.642 ± 0.028	3.902 ± 0.217	0.636	0.839	0.056	−2.133
	RH	0.961 ± 0.033	2.999 ± 0.289	0.483	0.915	0.275	−3.192
					0.891		−1.891

Table A1. *Cont.*

Basin	Variables Each 17,520 h	λ [bits]	Dc	S_k [bits/h]	H	LZ	<ΔI>
	Variables each 5399 h						
(ñ). Loncura Station (2016–2017, 3 masl)	CO	0.609 ± 0.084	2.189 ± 0.297	0.327	0.927	0.048	−2.023
	PM_{10}	0.184 ± 0.029	1.136 ± 0.058	0.284	0.835	0.031	−0.611
	$PM_{2.5}$	0.223 ± 0.032	1.848 ± 0.311	0.212	0.886	0.029	−0.740
					0.883		−1.125
	T	0.149 ± 0.025	1.083 ± 0.380	0.619	0.917	0.051	−0.495
	WS	0.718 ± 0.063	4.335 ± 0.060	0.331	0.927	0.066	−2.385
	RH	0.553 ± 0.039	4.741 ± 0.203	0.415	0.947	0.295	−1.837
					0.930		−1.572
	Variables each 17,520 h						
(o). Lota Rural Station (2016–2017, 16 masl)	CO	0.027 ± 0.009	1.997 ± 0.061	0.121	0.896	0.043	−0.090
	PM_{10}	0.366 ± 0.031	1.206 ± 0.341	0.305	0.890	0.242	−1.216
	$PM_{2.5}$	0.512 ± 0.030	1.603 ± 0.414	0.301	0.890	0.220	−1.701
					0.892		−1.002
	T	0.314 ± 0.023	1.396 ± 0.380	0.319	0.913	0.052	−1.043
	WS	0.068 ± 0.018	2.734 ± 0.034	0.202	0.843	0.038	−0.226
	RH	0.210 ± 0.020	1.857 ± 0.376	0.209	0.938	0.182	−0.698
					0.898		−0.656
	Variables each 22,248 h						
(p). Lagunillas (2021–2023, 2 masl)	CO	0.528 ± 0.071	3.092 ± 0.023	0.410	0.933	0.020	−1.754
	PM_{10}	0.347 ± 0.031	1.363 ± 0.432	0.252	0.899	0.344	−1.153
	$PM_{2.5}$	0.195 ± 0.015	1.481 ± 0.262	0.591	0.942	0.249	−0.648
					0.925		−1.185
	T	0.391 ± 0.021	1.391 ± 0.421	0.432	0.909	0.126	−1.300
	WS	0.717 ± 0.051	1.719 ± 0.254	1.081	0.933	0.028	−2.382
	RH	0.105 ± 0.013	0.371 ± 0.215	0.246	0.944	0.066	−0.349
					0.929		−1.344
	Variables each 22,248 h						
(q) El Escuadrón (2021–2023, 2 masl)	CO	0.606 ± 0.076	2.836 ± 0.041	0.436	0.933	0.014	−2.013
	PM_{10}	0.427 ± 0.026	1.575 ± 0.458	0.249	0.908	0.432	−1.418
	$PM_{2.5}$	0.517 ± 0.027	1.888 ± 0.496	0.255	0.909	0.403	−1.717
					0.916		−1.716
	T	0.366 ± 0.021	1.345 ± 0.306	0.236	0.916	0.110	−1.216
	WS	0.767 ± 0.050	4.541 ± 0.099	0.439	0.934	0.028	−2.548
	RH	0.376 ± 0.023	0.605 ± 0.043	0.298	0.900	0.190	−1.249
					0.916		−1.671

Appendix E

Anomalous Diffusion Conjecture

If we consider that there is a Kolmogorov entropy which varies in infinitesimal quantities in a very small time domain and that the Lyapunov exponent is associated with two trajectories whose separation in phase space is at its maximum (maximum diffusion), Figure A2 can be obtained.

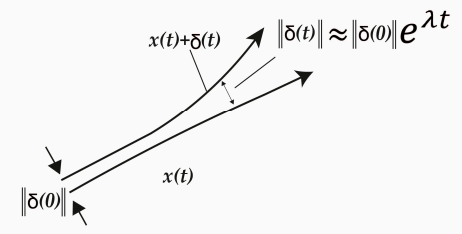


Figure A2. Variations in infinitesimal trajectories (x) and times (t) in a chaotic system.

If $x_P(t)$ and $x_{MV}(t)$ are separations between two trajectories of pollutants (P) and urban meteorology (MV) for two very small times (t_1 and $_{t2}$), then

$$a(t_1) = \frac{x_P(t_1)}{x_{0,P}} = e^{\lambda_P t_1} = e^{S_{K,P} t_1} \tag{A4}$$

$$a(t_2) = \frac{x_P(t_2)}{x_{0,P}} = e^{\lambda_P t_2} = e^{S_{K,P} t_2} \tag{A5}$$

$$a(t_1)a(t_2) \sim a^2 = e^{S_{K,P}(t_1+t_2)} = e^{S_{K,P} t'} \rightarrow a = e^{\frac{S_{K,P}}{2} t'} \tag{A6}$$

and

$$b(t_1) = \frac{x_{MV}(t_1)}{x_{0,MV}} = e^{\lambda_{MV} t_1} = e^{S_{K,MV} t_1} \tag{A7}$$

$$b(t_2) = \frac{x_{MV}(t_2)}{x_{0,MV}} = e^{\lambda_{MV} t_2} = e^{S_{K,MV} t_2} \tag{A8}$$

$$b(t_1)b(t_2) \sim b^2 = e^{S_{K,MV}(t_1+t_2)} = e^{S_{K,MV} t'} \rightarrow b = e^{\frac{S_{K,\,MV,}}{2} t'} \tag{A9}$$

Considering a and b at a time t'',

$$a(t'') = \frac{x_P(t'')}{x_{0,P}} = e^{S_{K,P} t''} \rightarrow t'' = \frac{\ln a(t'')}{S_{K,P}},\ b(t'') = \frac{x_{K,MV}(t'')}{x_{0,MV}} = e^{S_{K,MV} t''} \rightarrow t'' = \frac{\ln b(t'')}{S_{K,MV}} \tag{A10}$$

$$\ln\ b(t') = \frac{S_{K,VM}}{2} t' = \frac{S_{K,VM}}{2} \frac{\ln\ a(t'')}{S_{K,P}} = \frac{C_K}{2} \ln\ a(t'') \tag{A11}$$

According to the assumption of very small times $t' \sim t'' = t$, we obtain $b(t) = a^{\frac{C_K}{2}}$

$$\frac{x_{MV}(t)}{x_{0,MV}} = \left(\frac{x_P(t)}{x_{0,P}}\right)^{\frac{C_K}{2}} \rightarrow x_{MV}(t) = \frac{x_{0,MV}}{(x_{0,P})^{\frac{C_K}{2}}} (x_P(t))^{\frac{C_K}{2}} \tag{A12}$$

If the maximum spacing between phase space trajectories for the contaminating system is linear in time, $x_P(t) = v_P t$ (the trajectories are uniformly separated in time), then we obtain the following:

$$\begin{aligned} x_{MV}(t) &= \frac{x_{0,MV}}{(x_{0,P})^{\frac{C_K}{2}}} (v_P t)^{\frac{C_K}{2}} = \frac{x_{0,MV} v_P^{\frac{C_K}{2}}}{(x_{0,P})^{\frac{C_K}{2}}} t^{\frac{C_K}{2}} \\ &= K t^{\frac{S_{K,MV}}{2\,S_{K,P}}} \propto t^{\frac{S_{K,MV}}{2\,S_{K,P}}} \end{aligned} \tag{A13}$$

The variance of the quadratic displacement is as follows:

$$< x^2 > \ \propto t^{\frac{S_{K,MV}}{S_{K,P}}} = t^{C_K} \propto\ t^{\alpha} \tag{A14}$$

The quadratic diffusive variance associated with the displacement of the urban meteorology variables from the atmosphere to the interior of the boundary layer, close to the ground, is dependent on the interaction between the entropies of urban meteorology and the entropies of the pollutants according to the C_K quotient.

References

1. Mandelbrot, B. *The Fractal Geometry of Nature*, 2nd ed.; Times Books: New York, NY, USA, 1982.
2. Mandelbrot, B.; Van Ness, J.W. Fractional Brownian Motions, Fractional Noises and Applications. *SIAM Rev.* **1968**, *10*, 422–437. [CrossRef]

3. Falconer, K. The local structure of random processes. *J. Lond. Math. Soc.* **2003**, *67*, 657–672. [CrossRef]
4. Sprott, J.C. *Chaos and Time-Series Analysis*, 1st ed.; Oxford University Press: Oxford, UK, 2003.
5. Manríquez, R. Estructuras disipativas. De la termodinámica a la psicoterapia familiar. *Rev. Asoc. Esp. Neuropsiquiatría* **1987**, *VII*, 435–454.
6. Chen, Y. Normalizing and classifying shape indexes of cities by ideas from fractals. *Chaos Solitons Fractals* **2022**, *154*, 111653. [CrossRef]
7. Molinero, C. A Fractal Theory of Urban Growth. *Front. Phys.* **2022**, *10*, 861678. [CrossRef]
8. Chen, Y.G.; Wang, Y.H.; Li, X.J. Fractal dimensions derived from spatial allometric scaling of urban form. *Chaos Solitons Fractals* **2019**, *126*, 122–134. [CrossRef]
9. Cheng, Q. The perimeter-area fractal model and its application in geology. *Math. Geosci.* **1995**, *27*, 69–82. [CrossRef]
10. De Keersmaecker, M.-L.; Frankhauser, P.; Thomas, I. Using fractal dimensions for characterizing intra-urban diversity: The example of Brussels. *Geogr. Anal.* **2003**, *35*, 310–328. [CrossRef]
11. Dutton, G. Size and shape in the growth of human communities. *Ekistics* **1973**, *36*, 142–243.
12. Feng, J.; Chen, Y.G. Spatiotemporal evolution of urban form and land use structure in Hangzhou, China: Evidence from fractals. *Environ. Plan. B Plan. Des.* **2010**, *37*, 838–856. [CrossRef]
13. Frankhauser, P. *La Fractalité des Structures Urbaines (The Fractal Aspects of Urban Structures)*; Economic: Paris, France, 1994; ISBN 2-7178-2668-8.
14. Frankhauser, P. The Fractal Approach. A New Tool for the Spatial Analysis of Urban Agglomerations. *Popul. Engl. Sel.* **1998**, *10*, 205–240. Available online: http://www.jstor.org/stable/2998685 (accessed on 20 October 2023). [CrossRef]
15. Frankhauser, P. Fractal geometry for measuring and modeling urban patterns. In *The Dynamics of Complex Urban Systems: An Interdisciplinary Approach*; Albeverio, S., Andrey, D., Giordano, P., Vancheri, A., Eds.; Physica-Verlag: Heidelberg, Germany, 2008; pp. 213–243.
16. Voss, R.F. Random fractals: Characterization and measurement. In *Scaling Phenomena in Disordered Systems*; Plenum Press: New York, NY, USA, 1985; pp. 1–11.
17. Voss, R.F. Random Fractal Forgeries. In *Fundamental Algorithms for Computer Graphics*; Earnshaw, R.A., Ed.; NATO ASI Series; Springer: Berlin/Heidelberg, Germany, 1985; Volume 17. [CrossRef]
18. Cox, D.T.C.; Gaston, K.J. Human–nature interactions and the consequences and drivers of provisioning wildlife. *Phil. Trans. R. Soc. B* **2018**, *373*, 20170092. [CrossRef] [PubMed]
19. Holling, C.S. Resilience and Stability of Ecological Systems. *Annu. Rev. Ecol. Syst.* **1973**, *4*, 1–23. [CrossRef]
20. González, J.E.; Ramamurthy, P.; Bornstein, R.D.; Chen, F.; Bou-Zeid, E.R.; Ghandehari, M.; Luvall, J.; Mitra, C.; Niyogi, D. Urban climate and resiliency: A synthesis report of state of the art and future research directions. *Urban Clim.* **2021**, *38*, 100858. [CrossRef]
21. Stull, R.B. *Introduction to Boundary Layer Meteorology*; Kluwer Academic: Alphen an den Rijn, The Netherland, 1988; p. 666.
22. Yao, F.; Livneh, B.; Rajagopalan, B.; Wang, J.; Crétaux, J.F.; Wada, Y.; Berge-Nguyen, M. Satellites reveal widespread decline in global lake water storage. *Science* **2023**, *380*, 743–749. Available online: https://www.science.org/doi/10.1126/science.abo2812 (accessed on 20 October 2023). [CrossRef] [PubMed]
23. World Meteorological Organization. WMO-No. 1290, State of the Global Climate 2021. 2022. ISBN 978-92-63-11290-3. Available online: https://library.wmo.int/doc_num.php?explnum_id=11178 (accessed on 27 October 2023).
24. Rocque, R.J.; Beaudoin, C.; Ndjaboue, R.; Cameron, L.; Poirier-Bergeron, L.; Poulin-Rheault, R.A.; Fallon, C.; Tricco, A.C.; Witteman, H.O. Health effects of climate change: An overview of systematic reviews. *BMJ Open* **2021**, *11*, e046333. [CrossRef] [PubMed]
25. Tracey Areal, A.; Zhao, Q.; Wigmann, C.; Schneider, A.; Schikowski, T. The effect of air pollution when modified by temperature on respiratory health outcomes: A systematic review and meta-analysis. *Sci. Total Environ.* **2022**, *811*, 152336. [CrossRef] [PubMed]
26. Dai, J.; Chen, R.; Meng, X.; Yang, C.B.; Zhao, Z.; Kan, H. Ambient air pollution, temperature and out-of-hospital coronary deaths in Shanghai, China. *Environ. Pollut.* **2015**, *203*, 116–121. [CrossRef] [PubMed]
27. Anderson, C.A. Heat and violence. *Curr. Dir. Psychol. Sci.* **2001**, *10*, 33–38. [CrossRef]
28. Miles-Novelo, A.; Anderson, C.A. Climate Change and Aggression. Conference: Army Public Health Council Working Meeting on the Environmental Impacts on Mental Health 2019. Available online: https://www.researchgate.net/publication/354253705_Climate_Change_and_Aggression/citations (accessed on 14 September 2023).
29. Eliran Halali, E.; Meiran, N.; Shalev, I. Keep it cool: Temperature priming effect on cognitive control. *Psychol. Res.* **2017**, *81*, 343–354. [CrossRef]
30. Dyke, J.; Kleidon, A. The Maximum Entropy Production Principle: Its Theoretical Foundations and Applications to the Earth System. *Entropy* **2010**, *12*, 613–630. [CrossRef]
31. Liu, Y.; Liu, C.; Wang, D. Understanding Atmospheric Behaviour in Terms of Entropy: A Review of Applications of the Second Law of Thermodynamics to Meteorology. *Entropy* **2011**, *13*, 211–240. [CrossRef]
32. Mirzaei, P.A.; Haghighat, F. Approaches to study urban heat island–abilities and limitations. *Build. Environ.* **2010**, *45*, 2192–2201. [CrossRef]
33. Yuan, K.; Zhu, Q.; Riley, W.J.; Li, F.; Wu, H. Understanding and reducing the uncertainties of land surface energy flux parti-tioning within CMIP6 land models. *Agric. For. Meteorol.* **2022**, *319*, 108920. [CrossRef]

34. Yuan, K.; Zhu, Q.; Zheng, S.; Zhao, L.; Chen, M.; Riley, W.J.; Cai, X.; Ma, H.; Li, M.; Wu, H. Deforestation reshapes land-surface energy-flux partitioning. *Environ. Res. Lett.* **2021**, *16*, 024014. [CrossRef]
35. Balany, F.; Ng, A.W.; Muttil, N.; Muthukumaran, S.; Wong, M.S. Green Infrastructure as an Urban Heat Island Mitigation Strategy—A Review. *Water* **2020**, *12*, 3577. [CrossRef]
36. Black, S.; Minnett, D.; Parry, I.; Roaf, J.; Zhunussova, K. *A Framework for Comparing Climate Mitigation Effort across Countries*; Working Paper 2022/254; International Monetary Fund: Washington, DC, USA, 2022.
37. Fu, J.; Dupre, K.; Tavares, S.; King, D.; Banhalmi-Zakar, Z. Optimized greenery configuration to mitigate urban heat: A decade systematic review. *Front. Archit. Res.* **2022**, *11*, 466–491. [CrossRef]
38. Yang, L.; Qian, F.; Song, D.-X.; Zheng, K.-J. Research on Urban Heat-island Effect. *Procedia Eng.* **2016**, *169*, 11–18. [CrossRef]
39. Sun, Z.; Li, Z.; Zhong, J. Analysis of the Impact of Landscape Patterns on Urban Heat Islands: A Case Study of Chengdu, China. *Int. J. Environ. Res. Public Health* **2022**, *19*, 13297. [CrossRef]
40. Palma Behnke, R.; Barría, C.; Basoa, K.; Benavente, D.; Benavides, C.; Campos, B.; de la Maza, N.; Farías, L.; Gallardo, L.; García, M.J.; et al. *Chilean NDC Mitigation Proposal: Methodological Approach and Supporting Ambition*; Mitigation and Energy Working Group Report; COP25 Scientific Committee; Ministry of Science, Technology, Knowledge and Innovation: Santiago, Chile, 2019; Available online: https://mma.gob.cl/wp-content/uploads/2020/03/Mitigation_NDC_White_Paper.pdf (accessed on 15 January 2023).
41. Zhu, L.; Ge, X.; Chen, Y.; Zeng, X.; Pan, W.; Zhang, X.; Ben, S.; Yuan, Q.; Xin, J.; Shao, W.; et al. Short-term effects of ambient air pollution and childhood lower respiratory diseases. *Sci. Rep.* **2017**, *7*, 4414. [CrossRef]
42. Ferrelli, F.; Lujan, M.; Piccolo, M.C. Modificaciones en la distribución espacial de la temperatura y la humedad relativa como resultado del crecimiento urbano: El caso de la ciudad de Bahía Blanca. *Rev. Climatol.* **2016**, *16*, 51–61.
43. Pacheco, P.; Mera, E. Relations between Urban Entropies, Geographical Configurations, Habitability and Sustainability. *Atmosphere* **2022**, *13*, 1639. [CrossRef]
44. Chen, Y.; Wang, J.; Feng, J. Understanding the Fractal Dimensions of Urban Forms through Spatial Entropy. *Entropy* **2017**, *19*, 600. [CrossRef]
45. Martínez, J.A.; Vinagre, F.A. *La Entropía de Kolmogorov*; su Sentido Físico y su Aplicación al Estudio de Lechos Fluidizados 2D; Departamento de Química Analítica e Ingeniería Química, Universidad de Alcalá, Alcalá de Henares: Madrid, Spain, 2019; Available online: https://www.academia.edu/2479372 (accessed on 23 September 2022).
46. Singh, P.; Sharma, A.; Sur, U.; Rai, P.K. Comparative landslide susceptibility assessment using statistical information value and index of entropy model in Bhanupali-Beri región, Himachal Pradesh, India. *Environ. Dev. Sustain.* **2021**, *23*, 5233–5250. [CrossRef]
47. Fei, X.; Lou, Z.; Lv, X.; Ren, X.; Xiao, R. Pollution threshold assessment and risk area delineation of heavy metals in soils through the finite mixture distribution model and Bayesian maximum entropy theory. *J. Hazard. Mater.* **2023**, *452*, 131231. [CrossRef] [PubMed]
48. Hu, H.; Tan, Z.; Liu, C.; Wang, Z.; Cai, X.; Wang, X.; Ye, Z.; Zheng, S. Multi-timescale analysis of air pollution spreaders in Chinese cities based on a transfer entropy network. *Front. Environ. Sci.* **2022**, *10*, 970267. [CrossRef]
49. Alifa, M.; Castruccio, S.; Bolster, D.; Bravo, M.; Crippa, P. Information entropy tradeoffs for efficient uncertainty reduction in estimates of air pollution mortality. *Environ. Res.* **2022**, *212*, 113587. [CrossRef] [PubMed]
50. Pacheco, P.; Mera, E. Evolution over Time of Urban Thermal Conditions of a City Immersed in a Basin Geography and Mitigation. *Atmosphere* **2023**, *14*, 777. [CrossRef]
51. Pacheco, P.R.; Salini, G.A.; Mera, E.M. Entropía y neguentropía: Una aproximación al proceso de difusión de contaminantes y su sostenibilidad. *Rev. Int. Contam. Ambient.* **2021**, *37*, 167–185. [CrossRef]
52. Pacheco, P.; Mera, E.; Salini, G. Urban Densification Effect on Micrometeorology in Santiago, Chile: A Comparative Study Based on Chaos Theory. *Sustainability* **2022**, *14*, 2845. [CrossRef]
53. Dijkstra, H.A.; Viebahn, J.P. Sensitivity and resilience of the climate system: A conditional nonlinear optimization approach. *Commun. Nonlinear Sci. Numer. Simul.* **2015**, *22*, 13–22. [CrossRef]
54. Pacheco, P.; Mera, E.; Fuentes, V. Intensive Urbanization, Urban Meteorology and Air Pollutants: Effects on the Temperature of a City in a Basin Geography. *Int. J. Environ. Res. Public Health* **2023**, *20*, 3941. [CrossRef] [PubMed]
55. Pacheco, P.; Mera, E.; Fuentes, V.; Parodi, C. Initial Conditions and Resilience in the Atmospheric Boundary Layer of an Urban Basin. *Atmosphere* **2023**, *14*, 357. [CrossRef]
56. Farmer, J.D. Chaotic attractors of an infinite dimensional dynamical system. *Phys. D* **1982**, *4*, 366–393. [CrossRef]
57. Farmer, J.D.; Otto, E.; Yorke, J.A. The dimension of chaotic attractors. *Phys. D* **1983**, *7*, 153–180. [CrossRef]
58. Yu, B.; Huang, C.; Liu, Z.; Wang, H.; Wang, L. A chaotic analysis on air pollution index change over past 10 years in Lanzhou, northwest China. *Stoch. Environ. Res. Risk Assess.* **2011**, *25*, 643–653. [CrossRef]
59. Takens, F. Detecting strange attractors in turbulence. In *Dynamical Systems and Turbulence, Warwick, 1980*; Rand, D.Y., Young, L.S., Eds.; Springer: Berlin/Heidelberg, Germany, 1981.
60. Cao, L. Practical method for determining the minimum embedding dimension of a scalar time series. *Phys. D Nonlinear Phenom.* **1997**, *110*, 43–50. [CrossRef]
61. Wolf, A.; Swift, J.B.; Swinney, H.L.; Vastano, J.A. Determining Lyapunov exponents from a time series. *Phys. D* **1985**, *16*, 285–317. [CrossRef]
62. Grassberger, P.; Procaccia, L. Characterization of strange attractors. *Phys. Rev. Lett.* **1983**, *50*, 346–349. [CrossRef]

63. Kolmogorov, A.N. On Entropy per unit Time as a Metric Invariant of Automorphisms. In *Doklady Akademii Nauk SSSR*; Akademiia nauk SSSR: Moscow, Russia, 1959; Volume 124, pp. 754–755.
64. Sinai, Y.G. On the concept of entropy of a dynamical system. In *Doklady Akademii Nauk SSSR*; Akademiia nauk SSSR: Moscow, Russia, 1959; Volume 124, p. 768.
65. Pesin, Y.B. Characteristic Lyapunov exponents and smooth ergodic theory. *Russ. Math. Surv.* **1977**, *32*, 55–114. [CrossRef]
66. Kolmogorov, A.N. A new invariant for transitive dynamical systems. *Dokl. Akad. Nauk. Souiza Sovestkikh Sotsialisticheskikh Respuplik* **1958**, *119*, 861–864.
67. Ruelle, D. *Thermodynamic Formalism: The Mathematical Structures of Classical Equilibrium Statistical Mechanics*; Addison-Wesley Pub Co.: Reading, MA, USA, 1978.
68. Shaw, R. Strange attractors, chaotic behavior and information flow. *Z. Nat. A* **1981**, *36*, 80–112. [CrossRef]
69. Cohen, A.; Procaccia, I. Computing the Kolmogorov entropy from time signals of dissipative and conservative dynamical systems. *Phys. Rev. A* **1985**, *31*, 1872–1882. [CrossRef]
70. Han, W.; Li, Z.; Wu, F.; Zhang, Y.; Guo, J.; Su, T.; Cribb, M.; Fan, J.; Chen, T.; Wei, J.; et al. The mechanisms and seasonal differences of the impact of aerosols on daytime surface urban heat island effect. *Atmos. Chem. Phys.* **2020**, *20*, 6479–6493. [CrossRef]
71. SINCA (Sistema de Información Nacional de Calidad del Aire). Available online: https://sinca.mma.gob.cl/ (accessed on 13 April 2023).
72. SINAICA. 2022. Mexico, Sistema Nacional de Información de la Calidad del Aire. Available online: https://sinaica.inecc.gob.mx/ (accessed on 12 February 2023).
73. SUIA. 2022. Ecuador, Sistema Único de Información Ambiental. Available online: http://suia.ambiente.gob.ec/ambienteseam/home.seam (accessed on 14 January 2023).
74. Weiss, M.; Elsner, M.; Kartberg, F.; Nilsson, T. Anomalous subdiffusion is a measure for cytoplasmic crowding in living cells. *Biophys. J.* **2004**, *87*, 3518–3524. [CrossRef] [PubMed]
75. Shlesinger, M.F. Mathematical physics: Search research. *Nature* **2006**, *443*, 281–282. [CrossRef] [PubMed]
76. Hernandez-Herran, D.; Núñez López, M.; Velasco-Hernandez, J.X. Telegraphic double porosity models for head transient behavior in naturally fractured aquifers. *Water Resour. Res.* **2013**, *49*, 4399–4408. [CrossRef]
77. Buldyrev, S.V.; Goldberger, A.L.; Havlin, S.; Peng, C.K.; Stanley, H.E. Fractals in Biology and Medicine: From DNA to the Heartbeat. In *Fractals in Science*; Bunde, A., Havlin, S., Eds.; Springer: Berlin/Heidelberg, Germany, 1994. [CrossRef]
78. Masoliver, J.; Montero, M.; Weiss, G.H. Continuous-time random-walk model for financial distributions. *Phys. Rev. E* **2003**, *67*, 021112. [CrossRef] [PubMed]
79. Magré, O.; Guglielmi, M. Modelling and analysis of fractional Brownian motions. *Chaos Solitons Fractals* **1997**, *8*, 377–388. [CrossRef]
80. Sanaz, S.; Higgins, J.L.; Mannion, P.C.; Tamkun, M.M.; Krapf, D. Plasma Membrane is Compartmentalized by a Self-Similar Cortical Actin Meshwork. *Phys. Rev. X* **2017**, *7*, 011031. [CrossRef]
81. Cherstvy, A.G.; Chechkin, A.V.; Metzler, R. Anomalous diffusion and ergodicity breaking in heterogeneous diffusion processes. *New J. Phys.* **2013**, *15*, 083039. [CrossRef]
82. Lim, S.C.; Muniandy, S.V. Self-similar Gaussian processes for modeling anomalous diffusion. *Phys. Rev. E* **2002**, *66*, 021114. [CrossRef] [PubMed]
83. Krapf, D.; Metzler, R. Strange interfacial molecular dynamics. *Phys. Today* **2019**, *72*, 48–54. [CrossRef]
84. Manzo, C.; Garcia-Parajo, M.F. A review of progress in single particle tracking: From methods to biophysical insights. *Rep. Prog. Phys.* **2015**, *78*, 124601. [CrossRef] [PubMed]
85. Yoav, S.; Miri, B.; Ido, A.; Nir, D. Observation of Anomalous Diffusion and Fractional Self-Similarity in One Dimension. *Phys. Rev. Lett.* **2012**, *108*, 093002. [CrossRef]
86. Bronshtein, I.; Israel, Y.; Kepten, E.; Mai, S.; Shav-Tal, Y.; Barkai, E.; Garini, Y. Transient anomalous diffusion of telomeres in the nucleus of mammalian cells. *Phys. Rev. Lett.* **2009**, *103*, 018102. [CrossRef]
87. Weigel, A.V.; Simon, B.; Tamkun, M.M.; Krapf, D. Ergodic and nonergodic processes coexist in the plasma membrane as observed by single-molecule tracking. *Proc. Natl. Acad. Sci. USA* **2011**, *108*, 6438–6443. [CrossRef] [PubMed]
88. Regner, B.M.; Vučinić, D.; Domnisoru, C.; Bartol, T.M.; Hetzer, M.W.; Tartakovsky, D.M.; Sejnowski, T.J. Anomalous Diffusion of Single Particles in Cytoplasm. *Biophys. J.* **2013**, *104*, 1652–1660. [CrossRef]
89. Sabri, A.; Xu, X.; Krapf, D.; Weiss, M. Elucidating the Origin of Heterogeneous Anomalous Diffusion in the Cytoplasm of Mammalian Cells. *Phys. Rev. Lett.* **2020**, *125*, 058101. [CrossRef]
90. Jeon, J.-H.; Leijnse, N.; Oddershede, L.B.; Metzler, R. Anomalous diffusion and power-law relaxation of the time averaged mean squared displacement in worm-like micellar solutions. *New J. Phys.* **2013**, *15*, 045011. [CrossRef]
91. Georgiev, S.; Vulkov, L. Parameters Identification and Numerical Simulation for a Fractional Model of Honeybee Population Dynamics. *Fractal Fract.* **2023**, *7*, 311. [CrossRef]
92. Einstein, A. Über die von der molekularkinetischen Theorie der Wrme geforderte Bewegung von in ruhenden Flssigkeiten suspendierten Teilchen. *Ann. Phys.* **1905**, *322*, 549–560. [CrossRef]
93. Matheron, G.; De Marsily, G. Is Transport in Porous Media Always Diffusive, a Counterexample. *Water Resour. Res.* **1980**, *16*, 901–917. [CrossRef]

94. Gelhar, L.W.; Mantoglou, A.; Wlty, C.; Rehfeldt, K.R. A Review of Field-Scale Physical Solute Transport Processes in Saturated and Unsaturated Porous Media. Research Project 2485-5 1985, MIT, Cambridge Massachusetts 02139. Available online: https://www.nrc.gov/docs/ML0331/ML033100477.pdf (accessed on 5 August 2023).
95. Vainstein, M.H.; Costa, I.V.L.; Oliveira, F.A. Mixing, Ergodicity and the Fluctuation-Dissipation Theorem in complex systems. *arXiv* **2005**. [CrossRef]
96. Metzler, R.; Klafter, J. The random walk's guide to anomalous diffusion: A fractional dynamics approach. *Phys. Rep.* **2000**, *339*, 1–77. [CrossRef]
97. Zhang, Y.; Benson, D.A.; Meerschaert, M.M.; LaBolle, E.M.; Scheffler, H.-P. Random walk approximation of fractional order multiscaling anomalous diffusion. *Phys. Rev. E* **2006**, *74*, 039901. [CrossRef]
98. Chaves, A.S. A fractional diffusion equation to describe Lévy flights. *Phys. Lett. A* **1998**, *239*, 13–16. [CrossRef]
99. Sprott, J.C. *Chaos Data Analyzer Software, Version 2.1*; EEUU: Madison, WI, USA, 1995; Available online: https://sprott.physics.wisc.edu./cda.htm (accessed on 7 January 2023).
100. Havlin, S.; Ben-Avraham, D. Diffusion in disordered media. *Adv. Phys.* **2002**, *51*, 187–292. [CrossRef]
101. Balcerek, M.; Wyłomańska, A.; Burnecki, K.; Metzler, R.; Krapf, D. Modelling intermittent anomalous diffusion with switching fractional Brownian motion. *arXiv* **2023**. [CrossRef]

Disclaimer/Publisher's Note: The statements, opinions and data contained in all publications are solely those of the individual author(s) and contributor(s) and not of MDPI and/or the editor(s). MDPI and/or the editor(s) disclaim responsibility for any injury to people or property resulting from any ideas, methods, instructions or products referred to in the content.